Late Quaternary tephrostratigraphy and cryptotephrostratigraphy of core MD012422: Improving marine tephrostratigraphy of the NW Pacific

Tabito Matsu'ura [a, *], Minoru Ikehara [b], Tatsuyuki Ueno [c]

[a] Regulatory Standard and Research Department, Secretariat of Nuclear Regulation Authority (S/NRA/R), 1-9-9 Roppongi, Minato-ku, Tokyo, 106-8450, Japan
[b] Center for Advanced Marine Core Research, Kochi University, 200 Monobe-otsu, Nankoku, Kochi, 783-8502, Japan
[c] Faculty of Science and Engineering, Kokushikan University, 4-28-1 Setagaya, Setagaya-Ku, Tokyo, 154-8515, Japan

ARTICLE INFO

ABSTRACT

We investigated the deep-sea sedimentary sequence of core MD012422 corresponding to the last 350 ka (since marine isotopic stage, MIS 10) from off Shikoku Island, NW Pacific Ocean, and refined its tephrostratigraphy. We detected many tephras and cryptotephras and correlated them with terrestrial tephras on the basis of the major- and trace-element compositions of their glass shards. Then we cross-checked our results against the reported marine tephrostratigraphy in the NW Pacific area and assessed the relative timing of tephra eruptions and bioevents. Many widespread tephras and cryptotephras originated from the Kyushu volcanic zone (Kuju, Aso, Kakuto, Aira, Ata, and Kikai volcanoes/calderas), along with the Takayama-Ng1 tephra (Tky-Ng1) from Suiendani volcano in central Honshu, were detected in the core. These tephras were used to validate and refine the reported NW Pacific marine tephrostratigraphy and to develop useful time-synchronous markers for this ocean area. Among the tephras, Ata-Torihama (Ata-Th) occurs at the MIS 7/8 transition (ca. 240 ka) and its horizon overlaps with a calcareous nannofossil biohorizon, the first appearance datum (FAD) of *Emiliania huxleyi*. Ata-Th and this biohorizon are stratigraphically above the Tky-Ng1 (MIS 8/9 transition, 290−300 ka) and Kakuto (Kkt, MIS 9/10 transition, 330−340 ka) tephras, and these tephras have the same stratigraphic relationship with this biohorizon in deep-sea sediments from the East China Sea, off Shikoku Island, and off central Honshu. However, in deep-sea cores from off northern Honshu, an inconsistency between the tephrostratigraphy and the FAD of *E. huxleyi* has been reported. This inconsistency can be explained by poor preservation of calcareous fossils in the deep waters off northern Honshu, which are more corrosive to calcium carbonate than the shallower waters off Shikoku Island. These findings emphasize the importance of cross-checking biohorizons against tephra horizons and of linking tephras between terrestrial and marine sequences to assess the synchronicity of globally correlated age indicators.

© 2021 The Author(s). Published by Elsevier Ltd. This is an open access article under the CC BY license (http://creativecommons.org/licenses/by/4.0/).

1. Introduction

Tephras are well-known, time-synchronous markers in ice cores and marine and terrestrial sedimentary records separated by long distances, because the eruption of a tephra is geologically instantaneous and fallout can occur at long distances from the source; thus, they are useful for assessing the relative timing of environmental changes (e.g., Lowe, 2011; Davies et al., 2014; Blockley et al., 2014; Rasmussen et al., 2014). In particular, compilations of hemispherically distributed intercontinental tephras (Lane et al., 2017) can provide reliable isochrons within sediments at many locations, thereby improving chronological models. Fallout tephras that are distributed mainly in ocean areas (i.e., transoceanic marine tephras) are similarly useful for synchronizing marine sequences between distant ocean areas.

Late Pleistocene tephras originated from the Kyushu volcanic zone are widely distributed in the volcanic arc regions of Japan, on the Asian continent, and in the waters of the Pacific Ocean, Japan Sea, and East China Sea (Fig. 1a and b). These tephras have been correlated and dated by using stratigraphic information and

radiometric dating techniques (e.g., Machida and Arai, 2003). Recently, the major- and trace-element compositions of glass shards in tephras present in cores SG06 and SG14 (high-resolution lacustrine archives covering the last 150 ky in central Japan) have been well characterized, providing reliable information for tephra correlation; further, these tephras are well dated by varve stratigraphy, ^{14}C, and Ar–Ar dating techniques (Smith et al., 2011, 2013; McLean et al., 2016, 2018, 2020; Albert et al., 2018, 2019). Albert et al. (2019) used these Late Pleistocene tephras to cross-check and refine the previously reported tephrostratigraphy of deep-sea sediments in the Izu-Bonin arc (Holes U1436A and U1437B; Schindlbeck et al., 2018) and East China Sea (Hole U1429; Sagawa et al., 2018). However, not only Late Pleistocene tephras but also

Middle Pleistocene tephras need to be developed for use as time-synchronous markers in this ocean area.

The MD012422 site off Shikoku Island is situated in the non-volcanic forearc, about 280 km from the volcanic front on Kyushu Island. Because this site is downwind of the Kyushu volcanic zone, it receives tephras erupted from volcanoes on Kyushu Island (Ikehara et al., 2006, Fig. 1b). MD012422 core sediments are associated with $\delta^{18}O$ stratigraphy corresponding to the last 350 ky (marine isotope stage [MIS] 9 to MIS 10 transition; Ikehara et al., 2006: Fig. 2); the core thus contains sediments older than the oldest sediments in cores SG06 and SG14. Glass shards and mineral grains in the reported tephras in this core have already been characterized by their refractive indices (Ikehara et al., 2006) but not yet by their major-
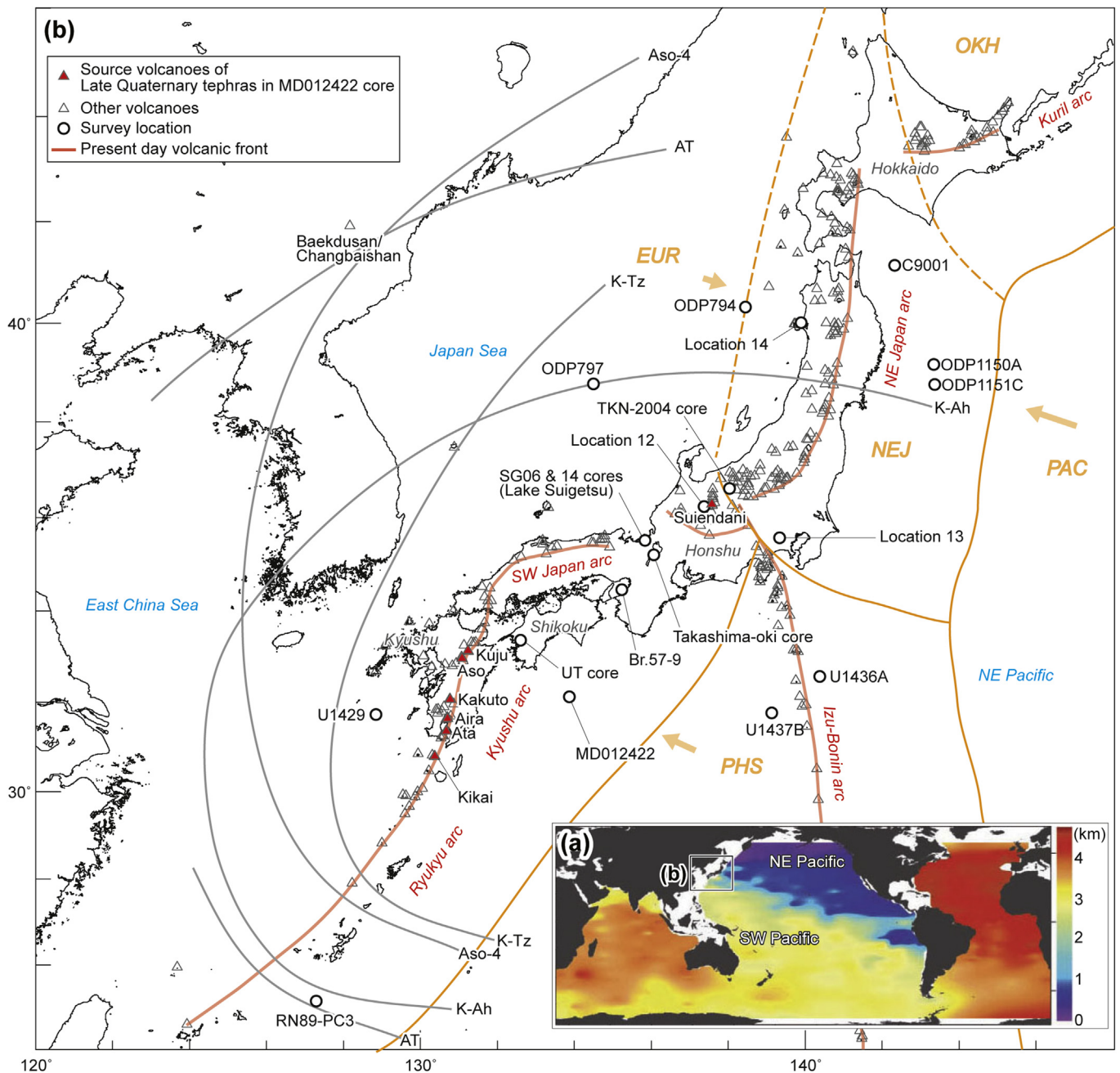
Fig. 1. (a) Study area (NW Pacific) shown on a map of calcite saturation depth (Feely et al., 2004). (b) Locations of volcanoes, survey sites, ocean drilling sites, and tephra isopachs. PAC, Pacific plate; PHS, Philippine Sea plate; EUR, Eurasian plate; OKH, Okhotsk plate. The dashed lines indicate the Eurasian and Okhotsk plate boundaries proposed by Seno et al. (1996), and the area between them is the NE Japan block (NEJ), a possible microplate.
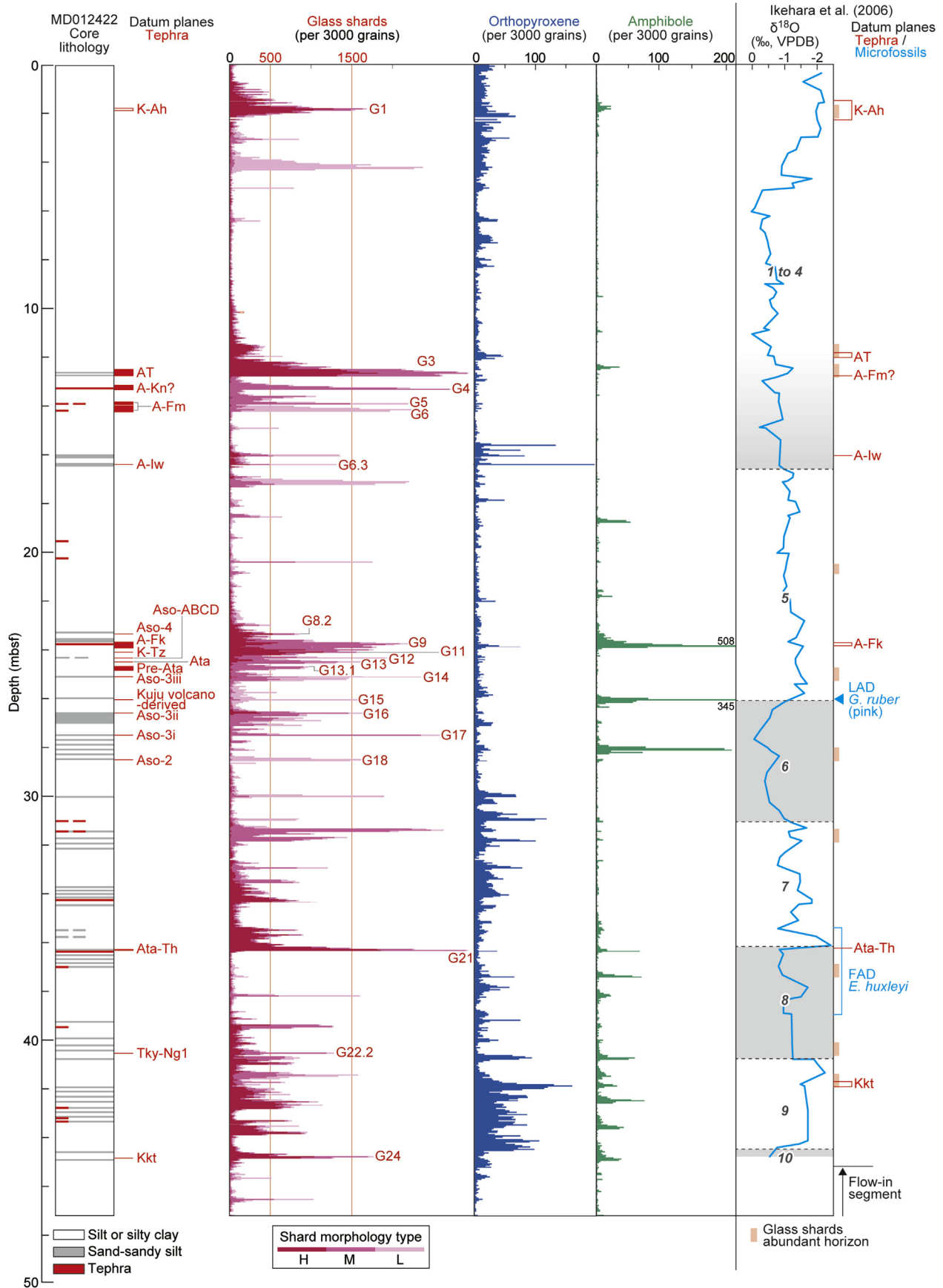
Fig. 2. Stratigraphy, datum planes, tephra grain components, and the oxygen isotopic record of the planktonic foraminifer *Globigerinoides ruber* in core MD012422. The δ18O record with the stratigraphic positions of the last appearance datum (LAD) of *G. ruber* (pink) and the first appearance datum (FAD) of *Emiliania huxleyi* is from Ikehara et al. (2006). Tephra

and trace-element compositions; as a result, many tephras in the core have not been sufficiently well characterized for correlation with known tephra eruptions. Further, to establish an improved tephrostratigraphy for the core, all core sections need to be examined for cryptotephras (concentration horizons of tephra-derived particles that do not form visible tephra layers in the sediments). The core MD012422 tephrostratigraphy and cryptotephrostratigraphy can potentially provide useful age indicators for both the Late and Middle Pleistocene in marine sequences that include tephras originated from the Kyushu volcanic zone in the NW Pacific Ocean, East China Sea, and Japan Sea (Fig. 1b). In fact, the late Quaternary tephrostratigraphy and cryptotephrostratigraphy of deep-sea sequences have already been successfully developed for Holes C9001C, ODP1150A, and ODP1151C, all off Northern Honshu in the NW Pacific area (Matsu'ura et al., 2014, 2017, 2018; Matsu'ura and Komatsubara, 2017, 2018).

In the marine realm, glass shard concentrations can result from not only tephra falls but also redeposition, including reworking and bioturbation of previously deposited tephras (Allan et al., 2008; Griggs et al., 2014; Hopkins et al., 2015; Abbott et al., 2018). Further, because marine tephras may have been transported from distant areas not only in the air but also by oceanic currents or ice rafts (e.g., Griggs et al., 2014; Abbott et al., 2018), the glass shards in a single tephra horizon may derive from multiple sources; thus, their major- and trace-element distributions may not be unimodal but multimodal. Therefore, to establish a reliable tephrostratigraphy, it is important to discriminate in situ tephras from reworked tephras.

In this study, we investigated deep-sea sediments from core MD012422 to develop the tephrostratigraphy and cryptotephrostratigraphy of the core. We identified tephra and cryptotephra horizons by examining concentrations of glass shards in the core sediments where possible. We also sampled possibly correlative terrestrial tephras for comparison. Then we analyzed the major- and trace-element compositions of the glass shards and correlated the tephras and cryptotephras of the core with the terrestrial tephras. Further, we used these results to cross-check and reconsider previously reported tephra correlations in deep-sea sediments of the NW Pacific Ocean and East China Sea. We also cross-checked the tephrostratigraphy against the biostratigraphy of deep-sea sediments in these ocean areas.

2. Regional setting and overview of core MD012422

2.1. Regional setting

The Japanese Islands are located in the Kuril−Japan subduction zone, which comprises the Kuril, NE Japan, Izu-Bonin, SW Japan, Kyushu, and Ryukyu Island arcs (Fig. 1b). Each arc is divided into forearc (non-volcanic arc) and backarc (volcanic arc) areas by a volcanic front. Many tephras erupted during the Quaternary from volcanoes on the western side of the volcanic front on Kyushu Island (Fig. 3) are widely distributed, covering broad areas of the Japanese Islands, Pacific Ocean, Japan Sea, East China Sea, and the Asian continent (Machida and Arai, 2003, Fig. 1b). The rim morphology of Aso, Kakuto, and Aira calderas, which produced the widespread Aso-4 to −1 (87−270 ka), Kakuto (Kkt, 330−340 ka), and Aira-Tn (AT, 30 ka) tephras, respectively, is well preserved (Fig. 3), but that of Kobayashi caldera, which produced the Kobayashi-Kasamori tephra (Kb-Ks, 520−530 ka), is poorly

preserved (Fig. 3). The rim of Ata caldera, which produced the Ata and Ata-Torihama tephras (Ata, 100 ka; Ata-Th, 240 ka), is below sea level, and its morphology is well preserved (Matsumoto and Ui, 1997: Fig. 3). Similarly, Kikai caldera (Fig. 1b), which produced the Kikai-Akahoya (K-Ah, 7 ka) and Kikai-Tozurahara (K-Tz, 95 ka) tephras, is below sea level, but its rim morphology is well preserved, as shown by bathymetric data (Tatsumi et al., 2018).

2.2. Overview of previous work on the stratigraphy and age model of core MD012422

The MD012422 core site is on the continental slope off Shikoku Island at 2737 m water depth (32.1450°N, 133.8633°E; Ikehara et al., 2006, Fig. 1b). Core MD012422 is a giant piston core retrieved by R/V *Marion Dufresne* with a recovery rate of almost 100% (Ikehara et al., 2006). The core contains a continuous 47.3-m-long record of the marine sedimentary succession, which consists predominantly of silts or sandy silts that contain tephras and microfossils (Ikehara et al., 2006, Fig. 2). Ikehara et al. (2006) reported the following tephras and biohorizons in the MD012422 core sediments: from top to bottom, K-Ah (2.24 mbsf), AT (12.05 mbsf), Aira-Fukaminato (A-Fm: 12.78 mbsf), Aira-Iwato (A-Iw: 16.04 mbsf), Aira-Fukuyama (A-Fk: 23.89 mbsf), Ata (25.11 mbsf), last appearance datum (LAD) of *Globigerinoides ruber* (pink) (ca. 26 mbsf), Ata-Th (36.14 mbsf), first appearance datum (FAD) of *Emiliania huxleyi* (36−39 mbsf), and Kkt (42.08 mbsf). All of these tephras were erupted from volcanoes on Kyushu Island (Fig. 1b). The age model for core MD012422 reported by Ikehara et al. (2006) is constrained by ^{14}C ages of *Globorotalia inflata*, by dated tephras and biohorizons, and by the MIS boundary (MIS 9/10, 350 ka) inferred from the δ^{18}O stratigraphy, which occurs at the bottom of the sequence. According to this age model, the sedimentation rates in the upper and lower parts of the core (0−13 and 13−47.3 mbsf, respectively, corresponding to 0−30 ka and before 30 ka, respectively) were 20−70 cm/ky and about 10 cm/ky, respectively (Ikehara et al., 2006). Mechanical elongation during coring, inferred from the magnetic susceptibility anisotropy, may be the cause of the apparent high sedimentation rate in the upper part of the core (Ikehara et al., 2006).

3. Materials and methods

3.1. Sampling, laboratory procedures, and microscopic examination

We obtained samples from the working halves of sections 1 to 25 of core MD012422 (Ikehara et al., 2006). We sampled the tephras according to their thickness. We sampled thick (≥5 cm) layers of tephras and other sediments at 5-cm intervals from the top to the bottom of the core. However, when we identified a boundary between a tephra and other sediments within a 5-cm interval, we sampled them separately, if each was 2.5 cm thick; otherwise, if the tephra or the other sediments at the top (or bottom) of an interval that included a boundary was thinner than 2.5 cm, we combined it with the sample above (or below) having the same lithology. As a result, the sample on one side of the boundary could be almost 7.5 cm thick, whereas that on the other side would be between 2.5 and 5 cm thick. We collected a total of 945 samples, including 20 tephra and tephric samples (i.e., ash, sediments with very small ash patches, scattered ashy particles, etc.), from the MD012422 core

abbreviations: K-Ah, Kikai-Akahoya; AT, Aira-Tn; A-Kn, Aira-Kenashino; A-Fm, Aira-Fukaminato; A-Iw, Aira-Iwato; A-Fk, Aira-Fukuyama; K-Tz, Kikai-Tozurahara; Kuju, Kuju-volcano derived tephra; Ata-Th, Ata-Torihama; Tky-Ng1, Takayama-Ng1; Kkt, Kakuto. Only glass shard spikes and subspikes that have been correlated to known tephras, or for which a source volcano has been suggested, are labeled. Glass shard morphology is classified into types H, M, and L, corresponding to highly, moderately, and poorly vesiculated shards, respectively (see Supplementary material 7 for illustrations of shard morphological types). (For interpretation of the references to colour in this figure legend, the reader is referred to the Web version of this article.)
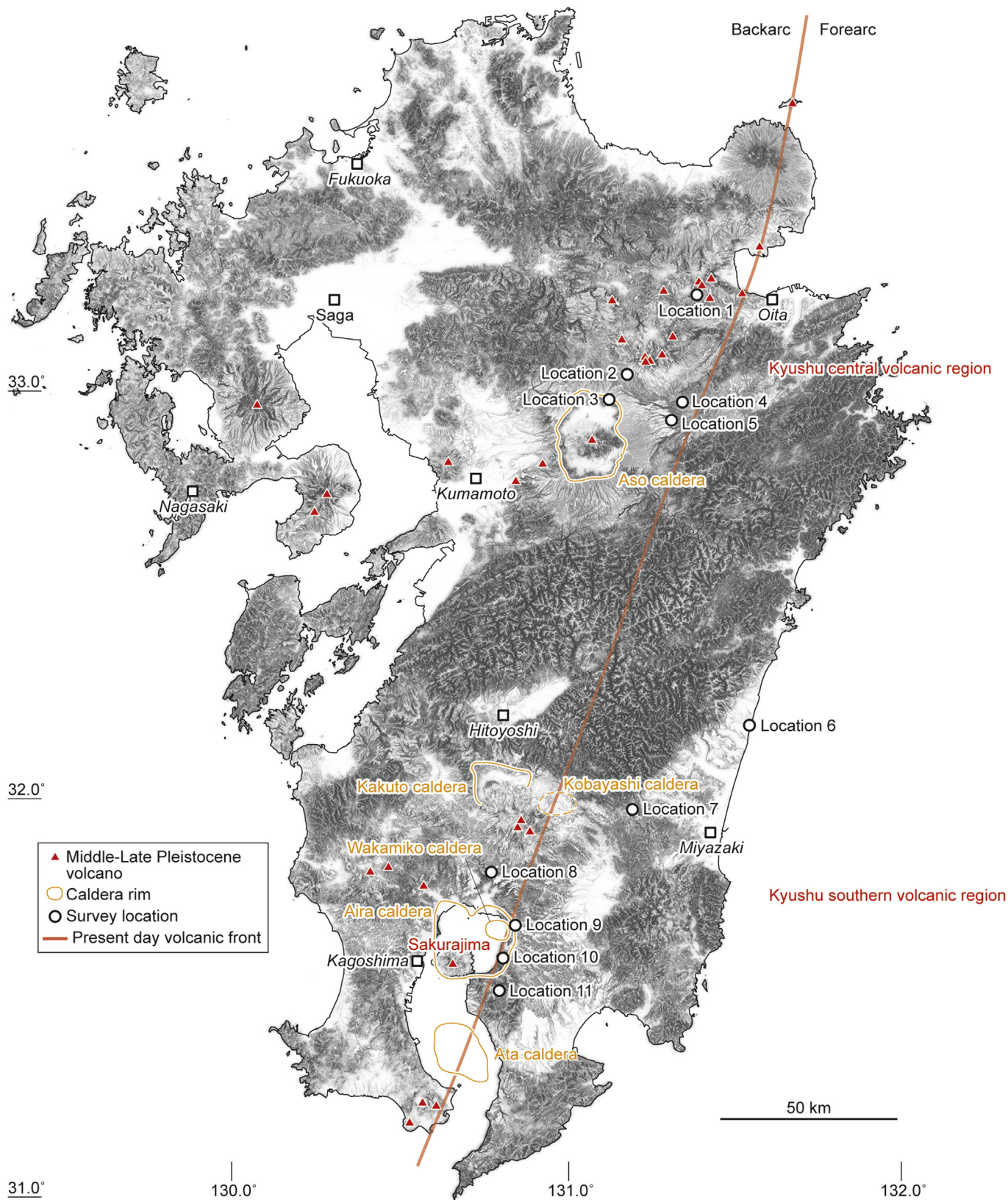
Fig. 3. Locations of late Quaternary volcanoes and calderas and survey sites on Kyushu Island. Late and Middle Pleistocene volcanoes and calderas are from AIST (2019).

sediments. We also sampled terrestrial tephras that we considered to be possible correlatives of the marine tephras from outcrops where they had been previously reported. All samples were sieved under running water through disposable 0.125-mm and 0.0625-mm sieves, which were changed between samples to prevent any contamination. The residues between 0.125 mm and 0.0625 mm in size were dried, embedded in resin, and mounted on slides. We then counted all grains on each slide under a polarizing microscope until a total of 3000 grains and tephra had been counted to determine the tephric and mineral grain assemblage.

To distinguish tephras and cryptotephras within the sediment record, we first picked out samples with high glass shard concentrations (more than 1500 glass shards per 3000 grains in core MD012422) (hereafter, high-concentration samples are referred to as "spikes"), and we assigned them whole-integer numbers from the top to the bottom of the core (e.g., G1, G2, …). For glass shard concentrations (defined as having fewer than 1500 shards per 3000 grains) between the whole-integer spikes, we identified concentrations of more than 300 glass shards per 3000 grains as subspikes and assigned them whole-integer plus decimal numbers from the top to the bottom of the core (e.g., G1.1, G1.2, …). We applied the same thresholds for spikes that we previously applied to deep-sea cores off the Japanese Islands, but because the background concentrations of glass shards differed among the cores, we applied different thresholds for subspikes: 300 shards per 3000 grains for Hole C9001C (Matsu'ura et al., 2014; 2017); and 500 shards per 3000 grains for Holes ODP1150A and ODP1151C (Matsu'ura et al., 2018) (Fig. 1b).

3.2. Compositional analysis

3.2.1. Major-element compositions

We carried out chemical analyses of the samples containing glass shard spikes and subspikes from core MD012422 and the terrestrial outcrops. We randomly extracted 10−15 glass shards from each spike or subspike and outcrop sample for these analyses. The major-element compositions of the glass shards were analyzed by using an energy-dispersive electron probe X-ray microanalysis (EDS-EPMA) system (Horiba Emax Evolution EX-270) at Furusawa Geological Survey. Major elements were measured by scanning a 4-μm grid of a targeted grain with a counting time of 50 s (EX-270), an accelerating voltage of 15 kV, and a beam current of 0.3 nA. The $\phi(\rho z)$ procedure was applied to correct for atomic number, absorption, and fluorescence effects. We report the major-element compositions of the glass shards as percentages by weight. Measurement data obtained by the EDS-EPMA system were also checked against measurements of the NIST 620 glass standard and secondary standard glasses (MPI-DING ATHO-G and StHs6/80-G, provided by the Max Planck Institut fuer Chemie) (Jochum et al., 2006; Kuehn et al., 2011). Analytical raw data were filtered to remove measurements with totals of <93 wt% (e.g., McLean et al., 2020: Supplementary material 1). Chemical compositions (averages and standard deviations) of the sample populations are shown in Supplementary material 2.

Chemical ranges were compared by using a variety of elemental bi-plots. The most diagnostically useful elements for this study were SiO_2, K_2O, FeO* (= total iron), CaO, Na_2O, and Al_2O_3. Other elements (MgO, TiO_2, and MnO) were not diagnostic for tephra identification in this study; therefore, plots of these elements are not shown.

3.2.2. Trace-element compositions

The trace-element compositions of the glass shards were analyzed by laser ablation-inductively coupled plasma mass spectrometry (LA-ICP-MS; quadrupole ICP-MS Thermo Fisher Scientific

iCAP Qc coupled to a Teledyne LSX-213 G2+ 213 nm excimer LA system) at Furusawa Geological Survey. Analytical conditions and the monitored isotopes are given in Supplementary material 1. We used the Al content, determined by EDS-EPMA as Al_2O_3, as an internal standard because Al is the second-most abundant major element in the glass shards. Although Si is the most abundant major element, we did not use it as an internal standard because the analytical precision of LA-ICP-MS is lower for Si than for Al. Among measured trace-element compositions (Supplementary material 1), we made no use of the Cr, Cu, and Ni contents because their measurement resolution was low.

We normalized our trace-element data by primitive mantle values (Sun and McDonough, 1989) and used a spidergram to display, as a first approximation, the volcanic sources of the tephras. Then we examined all other trace elements to further characterize and discriminate individual tephras in eruptive units from the same source by using bi-plots of selected trace elements.

Trace-element compositions of glass shards from a glass spike or subspike in core MD012422 were occasionally heterogeneous (Supplementary material 1), indicating that shards in the spike/subspike were derived from separate batches of magma that later became mingled or from closely spaced eruptions, or that they might include reworked shards, possibly from multiple sources, transported by intense bottom currents (e.g., Lowe, 2011; Griggs et al., 2014; Abbott et al., 2018). Our analytical data (10−15 points per sample) are sufficient to detect unimodal and bimodal populations but not multimodal populations or arrays (e.g., four arrays identified among 718 shards from Toba tuff; Westgate et al., 2013). Therefore, we only attempted to interpret unimodal or bimodal trace-element distributions of shards in this study.

4. Glass shard chemistry of terrestrial tephra samples

Terrestrial tephras potentially in core MD012422, as indicated by previous isopach mapping (e.g., Machida and Arai, 2003) and reported marine tephrostratigraphy (Ikehara et al., 2006), together with their sources, correlated MISs, numerical ages, sample IDs, sample material, and grid references, are shown in Table 1 and Supplementary material 3, and the lithology and stratigraphy of the tephras are shown in Supplementary material 4. Shard major-element compositions are shown in a bi-plot of SiO_2 versus K_2O (Fig. 4a), and in bi-plots of FeO* versus CaO and of Na_2O versus Al_2O_2 (Supplementary material 5). A spidergram is used to show the shard trace-element compositions (Fig. 4b).

4.1. Tephras from volcanoes in Kyushu central volcanic region

The Kuju volcano group in Kyushu central volcanic region (Kyushu CVR: Fig. 3) produced the Kuju-1 Pumice (Kj-P1) and the Kuju-D (Kj-D), Kuju-Handa (Kj-Hd), Kuju-Shimosakata (Kj-Sm), and Kuju-Miyagi (Kj-m) tephras (Ono et al., 1977; Machida and Arai, 2003). Glass shards in tephras and pumices derived from Kuju volcano since 0.15 Ma (Kj-m eruption) are all rhyolitic (Supplementary material 5). Kj-Hd (ignimbrite) possibly corresponds to Kj-P1 (pumice fall) (Nagaoka and Okuno, 2014), but their relative stratigraphic positions are still unclear; therefore, we investigated only Kj-P1 as a possible candidate for a marine tephra at the distal MD012422 site. These tephras, together with Aso-4, A-Fk, and Ata-Th, are amphibole-rich tephras, a characteristic that distinguishes them from the many amphibole-free tephras derived from volcanoes on Kyushu Island. Kj-P1, Kj-D, Kj-Sm, and Kj-m shards are characterized by high SiO_2 content ranges (>77 wt%) and high K_2O (>3.6 wt%) (Fig. 4a). Although in our analytical results, the Kj-P1 shards were subtly offset from the other Kuju tephras, being slightly lower in both SiO_2 and K_2O, all of the Kuju tephras were

Table 1
Terrestrial tephras potentially at the MD012422 site sampled in this study, their source volcanoes/calderas, and their ages.

Source	Eruption	Tephra abbreviation	Sample ID	Tephra deposits	Sample material	MIS	Age (ka)	Age Ref.
Kyushu central volcanic region (CVR)								
Aso	Aso-4	Aso-4	1301	Ash fall	Ash	5b	86.8 to 87.3	b
	Aso-A	Aso-A	504	Pumice & ash fall	Ash, pumice	5c−5b	89.7 to 105.3	a, e
	Aso-B	Aso-B	503	Ash fall	Ash	ditto	ditto	a, e
	Aso-C	Aso-C	502	Pumice & ash fall	Ash, pumice	ditto	ditto	a, e
	Aso-D	Aso-D	501	Pumice & ash fall	Ash, pumice	ditto	ditto	a, e
	Aso-3	Aso-3	202	Ignimbrite	Ash, pumice	6/5	133	g, h
	Aso-3	Aso-3	601	Ignimbrite	Ash, pumice	ditto	ditto	g, h
	Aso-2	Aso-2	301	Ignimbrite	Scoria, ash	6	146	g
	Aso-1	Aso-1	1401	Ash fall	Ash	8	250 to 270	e
Kuju	Kuju-1	Kj-D	101	Ash fall	Ash	4	54 ± 1.6	a
		Kj-P1	102	Pumice & ash fall	Pumice, ash	ditto	ditto	a
	Kuju-Shimosakata	Kj-Sm	401	Ignimbrite	Ash, pumice		0.11 ± 0.04 Ma	d
	Kuju-Miyagi	Kj-m	201	Ignimbrite	Ash, pumice		0.15 ± 0.04 Ma	d
Kyushu southern volcanic region (SVR)								
Kakuto	Kakuto	Kkt	1001	Ignimbrite	Ash, pumice	9/10	330 to 340	e
Aira	Aira-Tn	AT	103	Ash fall	Ash	3	30.078 ± 0.096	a, k
	Aira-Ito Flow	A-Ito	8011	Ignimbrite	Ash, pumice	ditto	ditto	a, k
	Aira-Tsumaya S	A-TsS	8010	Ignimbrite	Ash, pumice	ditto	ditto	a, k
	ditto	ditto	809	ditto	Ash, pumice	ditto	ditto	a, k
	Aira-Osumi	A-Os	808	Pumice fall	Pumice	ditto	ditto	a, k
	Aira-Kenashino	A-Kn	807	Ash fall	Ash	ditto	29.545 to 30.437 (f) or 29 (i)	f, i
	Aira-Fukaminato	A-Fm	806	Pumice fall	Pumice	ditto	29.865 to 30.933 (f) or 31 (i)	f, i
	Aira-Otsuka	A-Ot	805	Pumice & ash fall	Pumice, ash	ditto	30.730 to 33.216 (f) or 32.5 (i)	f, i
	Aira-Iwato	A-Iw	704	Pumice fall	Pumice	ditto	55.4 to 58.0	c
	Aira-Iwato Flow	A-Iw Fl	804	Ignimbrite	Pumice, ash	ditto	ditto	c
	Aira-Iwato Fall	A-Iw Fa	803	Pumice fall	Pumice	ditto	ditto	c
	Aira-Fukuyama	A-Fk	901	Pumice fall	Pumice	5b/5c	90	e
Ata	Ata	Ata	802	Ignimbrite	Ash, pumice	5c/5d	99.3 ± 6.0	a, j
			801	Ignimbrite	Ash, pumice	ditto	ditto	a, j
	Ata-Torihama	Ata-Th	1002	Ignimbrite	Ash, pumice	7/8	240	e
Sakurajima	Sakurajima-Satsuma	Sz-S	1101	Pumice fall	Pumice	2	12.8	e
			1102	Pumice fall	Pumice	ditto	ditto	e
Kikai	Kikai-Akahoya	K-Ah	104	Ash fall	Ash	1	7.253 ± 0.046	a, k
	Kikai-Tozurahara	K-Tz	702	Ash fall	Ash	5c−5b	94.5 ± 4.8	a, e
Central Japan volcanic region								
Suiendani?	Takayama-Ng1	Tky-Ng1	1201	Pumice fall	Pumice	8/9	290 to 300	e

References: a, Albert et al. (2019); b, Aoki (2008); c, Ikehara et al. (2006); d, Kamata et al. (1998); e, Machida and Arai (2003); f, McLean et al. (2020); g, Nagahashi et al. (2004); h, Nagahashi et al. (2007); i, Nagaoka et al. (2001); j, Oba (1991); k, Smith et al. (2013).

generally similar. Further, they overlapped with K_2O-rich glass from Aira caldera in Kyushu southern volcanic region (SVR) (Fig. 4a). Tephra shards derived from Kuju volcano cannot be distinguished from ones derived from Aira caldera by only their major-element compositions, but they can be distinguished by their trace-element compositions, because among tephras from Kyushu Island, only the Kuju tephra series shows an adakitic signature (Albert et al., 2019; see below).

Aso caldera in Kyushu CVR (Fig. 3) produced the widespread Aso-4, Aso-ABCD, Aso-3, Aso-2, and Aso-1 tephras (Ono et al., 1977; Machida and Arai, 2003). In our analytical results, tephra shards from Aso caldera since Aso-1 eruption (mid MIS 8, 250−270 ka: Machida and Arai, 2003) ranged compositionally from trachydacite to rhyolite (Supplementary material 5). In addition, the K_2O contents of Aso-4, Aso-ABCD, Aso-2, and Aso-1 shards were high (>4 wt%), but Aso-3 shards had high (mode 1, >4.5 wt%) or moderate K_2O contents (mode 2, ca. 3.5 wt%) (Fig. 4a). These shard modes correspond to high (mode 1, ca. 70 wt%) and low (mode 2, ca. 62 wt%) SiO_2 content modes, respectively (Supplementary material 2). On the SiO_2 and K_2O bi-plot, the intercept of the Aso-3

compositional array on the K_2O axis is higher than that of the Aso-4 array and lower than that of the Aso-2 array (Fig. 4a). The properties of these arrays are consistent with results reported by Nagahashi et al. (2004). The Aso-3 tephra has been divided into subunits (Aso-3W, -3A, -3B, and 3C: Kaneko et al., 2015). The occurrence of Aso-3 mode 2 at location 6 (sample 601) indicates that at that location, Aso-3 corresponds to the upper ignimbrite subunit (Aso-3B: Kaneko et al., 2015), which includes low-SiO_2 (63−66 wt%) glass shards (Albert et al., 2019). On the other hand, sample 202, which included only mode 1 shards with higher SiO_2 and K_2O contents, is consistent in this respect with the Aso-3A ignimbrite subunit (Kaneko et al., 2015; Albert et al., 2019). Further, among these tephras, Aso-3 mode 2 and Aso-2 shards were characterized by high FeO* (>6.0 wt%) and high CaO (>4.4 wt%) (Supplementary material 5).

Kj-P1, Kj-Sm, and Kj-m shards contained much less Y than Sr, indicating that they are adakitic, and their rare earth element (REE) abundances are systematically low among tephras from Kyushu Island (Albert et al., 2019: Fig. 4b). Consistent with their K_2O content range, Aso-4, Aso-3 mode 1, and Aso-1 shards were
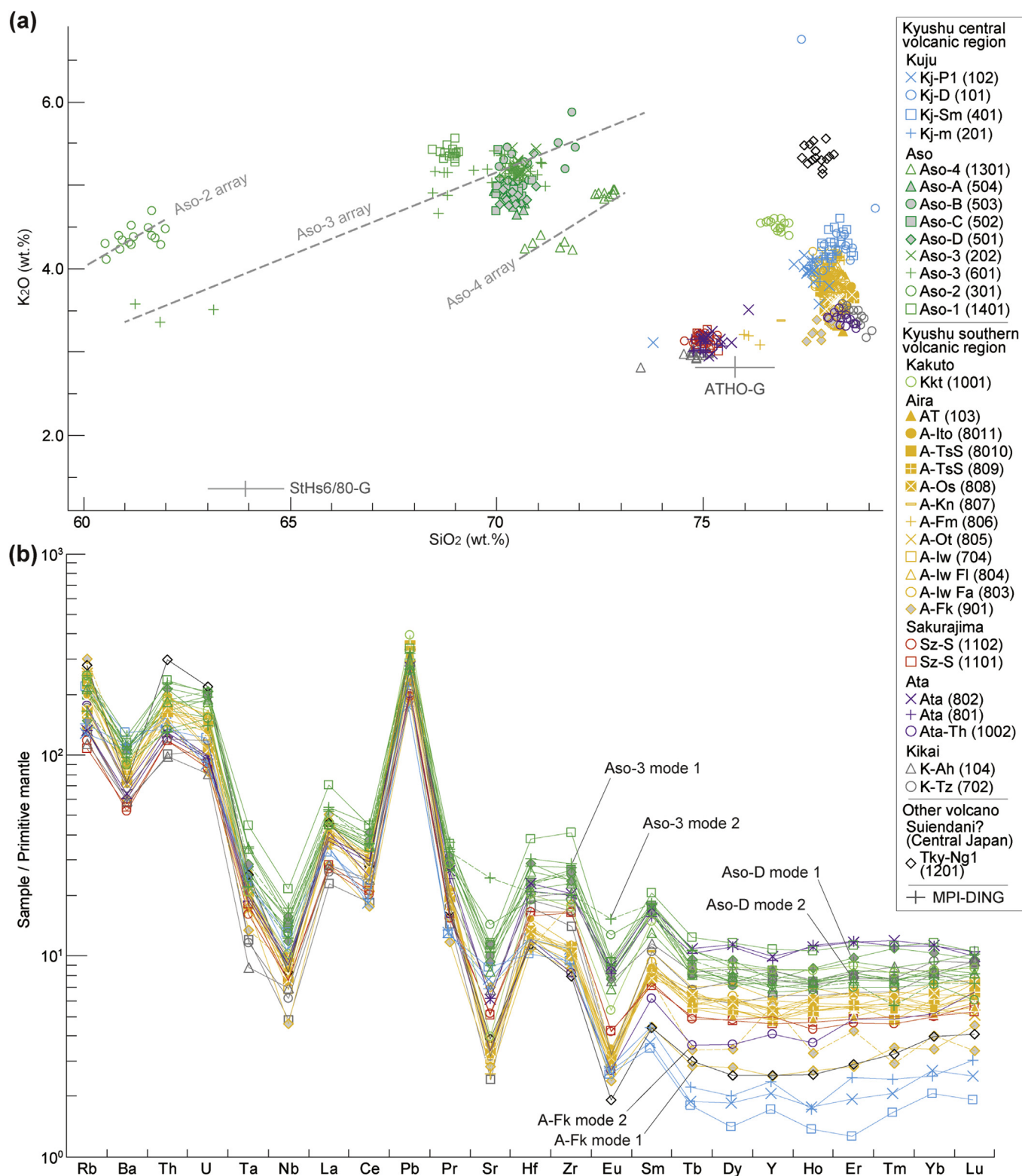
Fig. 4. Chemistries of glass shards in terrestrial tephras derived from volcanoes on Kyushu Island. (a) A bi-plot of SiO_2 and K_2O. Error bars on plots represent reproducibility, calculated as 2 SD of replicate analyses of MPI-DING ATHO-G and StHs6/80-G. (b) Spidergram showing trace-element compositions. In the key, the numbers in parentheses following the tephra names are sample IDs, the horizons of which are shown in stratigraphic sections in Supplementary material 4.

characterized by high contents of large-ion lithophile elements (LILE: Rb, Ba, etc.) and high-field-strength elements (HFSE: Th, U, etc.), and the REE abundances of these shards were systematically high among tephras from Kyushu Island (Fig. 4b; Supplementary material 2). On the other hand, Aso-3 mode 2 and Aso-2 shards had very high Sr and Eu contents, but otherwise their trace-element patterns were systematically lower than those of other Aso series tephras.

4.2. Tephras from volcanoes in Kyushu southern volcanic region

In Kyushu SVR (Fig. 3), glass shards derived from Kakuto, Aira, Sakurajima, Ata, and Kikai volcanoes/calderas since Kkt eruption (MIS 9, 330−340 ka: Machida and Arai, 2003) are all classified as rhyolitic (Supplementary material 5). The K_2O contents of these shards show the rough decreasing trend from north to south reported by Albert et al. (2019): from calderas Kakuto (Kkt, ca. 4.5 wt %) to Kikai (K-Ah, ca. 3.0 wt%) (Fig. 4a).

Glass shards in all samples of the Aira tephra series, except for A-Fk, were not distinguishable by their major-element compositions (Fig. 4a). A-Fk could be distinguished from the other tephras by its lower K_2O content range (Fig. 4a). Glass shards in Sz-S, from Sakurajima volcano, were similar to Ata shards in SiO_2 and K_2O contents, but they were characterized by high CaO and Al_2O_3 contents relative to those of Ata shards (Supplementary material 5). Ata and Ata-Th were derived from Ata caldera, but Ata shards were characterized by lower SiO_2 contents (<76 wt%) than Ata-Th shards (>78 wt%) (Fig. 4a). Ata-Th shards could be distinguished from K-Tz shards by their higher Al_2O_3 contents (Supplementary material 5), although shards from these two tephras overlapped on the bi-plots of SiO_2 and K_2O (Fig. 4a) and of FeO and CaO (Supplementary material 5). K-Tz shards were characterized by a higher SiO_2 content (>78 wt%) compared with K-Ah shards (<75 wt%) (Fig. 4a). In addition to these shard major-element compositions, A-Fk and Ata-Th included moderate to large amounts of amphibole grains, unlike all other Kyushu volcanic region tephras.

With regard to their trace-element pattern, Kkt shards generally plotted between Aso- and Aira-caldera-derived tephra shards (Fig. 4b); thus, the Kkt shard chemistry is consistent with the geographical location of Kakuto caldera between Kyushu CVR and SVR (Fig. 3). Glass shards of the Aira series tephras, except A-Fk, were characterized by higher LILE and HSFE contents relative to tephra shards from Sakurajima volcano and Ata and Kikai calderas (south of Aira caldera) (Fig. 4b). Different from the other Aira series tephras, A-Fk shards had bimodal trace-element content ranges, although the major elements were unimodally distributed. A-Fk modes 1 and 2 both showed systematically low HREE (Tb−Lu) abundances (Fig. 4b), and the Y content in particular of A-Fk mode 1 (11.49 ± 1.76 ppm) was similar to the Y contents of Kuju series tephras. However, A-Fk mode 1 shards were characterized by lower Ba content (421 ± 12 ppm) than shards of the Kuju tephra series (Kj-P1, 744 ± 83 ppm; Kj-Sm, 898 ± 34 ppm; Kj-m, 787 ± 57 ppm, respectively: Supplementary material 2). Among these tephras from Kyushu Island, Sz-S shards were characterized by very low LILE and HFSE content ranges (Fig. 4b). Ata and Ata-Th shards were systematically high and low in REE abundance, respectively (Fig. 4b); thus, they can be distinguished on this basis. Shards of both K-Ah and K-Tz were characterized by low Ta and Nb content ranges, as reported previously by Albert et al. (2019).

4.3. A tephra from a distant volcano

Tky-Ng1, which erupted from Suiendani volcano in central Honshu or another nearby volcano Tamura and Suzuki (2001), Fig. 1b), is found in terrestrial sediments on western Shikoku Island (Mizuno and Kikkawa, 1991; Tsuji et al., 2018), southwestward from the source. Therefore, Tky-Ng1 potentially occurs at the MD012422 site in the Pacific Ocean. The Tky-Ng1 age is 290−300 ka, based on stratigraphic information (Machida and Arai, 2003). Glass shards in Tky-Ng1 were classified as rhyolitic (Supplementary material 5). The shards were characterized by high SiO_2 content ranges (>77 wt %) and high K_2O (>5.1 wt%) (Fig. 4a). Consistent with their K_2O content range, the shards were also characterized high Rb and high Th content ranges (>146 and > 23.5 ppm, respectively)

(Supplementary material 1). Their REE abundances were systematically low compared with those of tephras from Kyushu CVR and SVR (Fig. 4b).

5. Characterization of tephra grains from core MD012422 and correlations with terrestrial tephras

We identified a total of 64 spikes and subspikes (24 spikes and 40 subspikes) that met our criteria for spikes and subspikes (see Section 3.1). The spike and subspike IDs and their depths, tephra-related core descriptions, amounts of tephra grains (shards and heavy minerals), and correlated tephras are shown in Table 2 and Supplementary material 6. The chemical compositions of all spikes and subspikes are given in Supplementary material 2, and those of spikes and subspikes confidently correlated to, or suggested as possible correlatives of known tephras, or for which a source volcano has been suggested, are in Table 3. Among the spikes and subspikes, spikes G4 and G9 and subspike G20.5 correspond to visible tephra layers, spike G21 occurs just above a visible tephra layer, and many spikes and subspikes appear to correspond to ash patches or scattered ashy particles in the core (Fig. 2). However, other spikes and subspikes do not correspond to visible tephra horizons, although several correspond just to coarse sediments (e.g., to sand layers or patches within a silty clay layer).

5.1. MIS 1 to 4 (present to 70 ka)

5.1.1. Spike G1 and Kikai Akahoya tephra

Spike G1 (1.81−1.91 mbsf) included a large amount of highly vesiculated (H-type; see Supplementary material 7) shards, but we did not observe any visible tephra in the corresponding horizon in our examination of the core (Table 2). The shards of spike G1 had wide SiO_2 and K_2O ranges, but most of them were similar to K-Ah shards from Kikai caldera (Fig. 5a). The occurrence of shards with a higher SiO_2 content, similar to that of AT shards (see below), indicates contamination. Most shards in spike G1 are also similar to K-Ah shards with respect to their FeO*, CaO, Na_2O, and Al_2O_3 content ranges (Supplementary material 5). Subspikes G0.1 and G0.2 are parts of the upward shard concentration tail (Fig. 2), and their shard major-element compositions are similar to that of G1 (Fig. 5a), indicating that their shards were reworked from the spike G1 horizon.

The shards of spike G1 are characterized by low Th and high Zr contents, similar to those of K-Ah (sample 104) analyzed in this study and reported by Albert et al. (2019) (Fig. 5b). Further, the trace-element contents of spike G1 and K-Ah are roughly similar, although the contents of some elements (e.g., Zn, Gd, Tb, Dy, Ho, Er, Yb, and Hf: Supplementary material 1) showed subtle differences, indicating heterogeneity of the original magma. Therefore, we correlate spike G1 with K-Ah, and spike G1 corresponds to the reported K-Ah horizon of 1.47−2.24 mbsf (Ikehara et al., 2006).

5.1.2. Spike G3 and Aira-Tn tephra

Spike G3 (12.50−12.81 mbsf) included a large amount of highly vesiculated (H-type) shards, and we observed fine sand but no visible tephra layer in this horizon in the core (Table 2). Most shards are similar to shards of the Aira tephra series, except A-Fk, with respect to their SiO_2 and K_2O content ranges (Fig. 5a) and their FeO*, CaO, Na_2O, and Al_2O_3 content ranges (Supplementary material 5). With respect to the large number of included H-type shards, Spike G3 is similar to AT, A-Ito, A-Ts, and A-Iw, all of which include many highly vesiculated shards, but it is dissimilar to A-Os, A-Kn, A-Fm, and A-Ot, which include many moderately or poorly vesiculated shards (M and L types; Supplementary material 7. Therefore, spike G3 may correlate with AT, A-Ito, A-Ts, or A-Iw. The spike G3

Table 2
Glass shard spikes and subspikes correlated to known tephras, or for which a source volcano has been suggested, in core MD012422, related core descriptions, glass shard morphologies, heavy mineral contents, and correlative tephras. Descriptions of visible tephra layers such as ash layers or ash patches are underlined. Amount ranges of glass shards (H, M and L types) and mineral grains (orthopyroxene [opx] and amphibole [amp]) are shown for spikes and subspikes that cover two or more sample horizons. All spikes and subspikes are included in Supplementary material 6.

Spike ID	Depth (mbsf)		Tephra-related core description	Glass shards			Heavy minerals		Correlated or suggested tephra
	Top	Bottom		H	M	L	Opx	Amp	
G1	1.81	1.91	None	1032 to 1275	361 to 463	45 to 48	21 to 22	13 to 24	K-Ah
G3	12.50	12.81	Contains sand at 12.67−12.68 m and 12.74−12.76 m.	1321 to 1815	746 −1263	17 to 122	1 to 13	1 to 7	AT
G4	13.26	13.35	Contains light gray ash layer at 13.31−13.345 m.	0	2055 to 2698	18 to 161	2 to 4	0 to 2	A-Kn?
G5	13.90	13.96	Contains ash patch (diameter: 0.8 cm)	0	1481	712	13	0	A-Fm
G6	14.10	14.26	Contains ash patch (diameter: 1.5 cm) at 14.20−14.26 m	0	86 to 305	1512 to 1925	2 to 11	0 to 1	A-Fm
G6.3	16.40	16.44	Contains sand patch at 16.40−16.42 m	250	245	820	199	0	A-Iw
G8.2	23.35	23.41	None	532	265	65	10	13	Aso-4
G9	23.71	23.95	Contains ashy sediments and ash layer at 23.80−23.84 m and 23.84 −23.89 m.	198 to 595	1005 to 1572	55 to 198	6 to 40	45 to 508	A-Fk
G11	24.10	24.15	None	1155	403	15	6	0	K-Tz
G12	24.35	24.37	Contains sand patch	122	1791	25	9	0	Aso-ABCD
G13	24.50	24.55	None	96	1231	281	13	2	Ata
G13.1	24.65	24.86	None	10 to 39	407 to 896	57 to 88	5 to 8	1 to 3	Pre-Ata
G14	25.11	25.15	Contains sandy sediments at 25.11−25.13 m and sand patch at 25.13 −25.15 m.	17 to 92	503 to 755	1112 to 1502	5 to 8	0 to 0.5	Aso-3iii
G15	26.05	26.10	None	2	132	1435	6	345	Kuju
G16	26.60	26.65	None	385	1075	170	15	1	Aso-3ii
G17	27.50	27.55	Contains sandy silt at 27.48−27.54 m.	13	2335	231	7	1	Aso-3i
G18	28.50	28.57	Contains blackish brown sandy silt.	3	26	1585	8	11	Aso-2
G21	36.30	36.38	Contains yellow layer at 36.38 m. An ash layer occurs at 36.38−36.41 m, just below spike G21.	1811 to 1855	437 to 1045	25	4 to 6	17 to 18	Ata-Th
G22.2	40.55	40.60	Contains dark brown fine sand patch at 40.58−40.60 m.	136	1056	88	5	5.5	Tky-Ng1
G24	44.80	44.85	Contains no tephric material but occurs above sandy silt at 44.89−45.05 m.	1045	655	67	6	15	Kkt

shards are characterized by slightly lower Th and higher Zr than shards of the proximal AT tephra series (from A-Os to A-Ito) and those of the A-Iw tephra (distal and proximal A-Iw flow and fall deposits) (Fig. 5b). Albert et al. (2019) differentiated AT and A-Iw by their Th and Zr content ranges, but in our samples the Th and Zr content ranges, though close to the reported ranges, partly overlap (Fig. 5b). Further, trace-element compositions of AT tephra series showed subtle differences in their U, Rb, Cs, and Pb contents (Supplementary material 1), indicating heterogeneity of the original magma or reflecting analytical uncertainty. On the basis of its U content especially, G3 is similar to A-Os (Fig. 5d), but this correlation is simply not supported by their glass shard morphologies (see above). We suggest, therefore, that spike G3 corresponds to the AT eruption sequence, but we cannot confidently correlate spike G3 to any proximal unit. The spike G3 horizon corresponds to the reported A-Fm horizon of 12.76−12.78 mbsf and is lower (by 0.5−1 m) than the reported AT horizon of 11.87−12.05 mbsf (Ikehara et al., 2006). We thus interpreted the reported A-Fm as original AT, and the reported AT as reworked AT.

5.1.3. Spikes G4, G5, and G6 and Aira-Kenashino, Aira-Fukaminato, and Aira-Otsuka tephras

Spikes G4 (13.26−13.35 mbsf), G5 (13.90−13.96 mbsf), and G6 (14.10−14.26 mbsf) included large amounts of moderately vesiculated M-type shards but, unlike spike G3, they did not include any H-type shards (Table 2; Supplementary material 7). We observed a light gray ash layer in the spike G4 horizon and a light gray ash patch in the spike G5 and G6 horizons, respectively (Table 2). Their glass shards are similar to shards of the Aira tephra series, except A-Fk, with respect to their SiO_2 and K_2O content ranges (Figs. 4a and 5a) and their FeO*, CaO, Na_2O, and Al_2O_3 content ranges

(Supplementary material 5). With respect to their K_2O content ranges (Fig. 5a; Supplementary material 2), G5 shards (4.05 ± 0.08 wt%) are more similar to A-Fm shards (4.09 ± 0.08 wt%) than to G6 shards (3.76 ± 0.14 wt%).

The shards of spikes G4−G6 are also similar to one other and to Aira tephra series shards with respect to their Th and Zr contents (Fig. 5c), but shards of spikes G5 and G6 are characterized by higher U than shards of spike G4, and they are similar to A-Fm shards rather than to A-Kn shards (Fig. 5e). However, the U contents did not differ between A-Fm and A-Kn tephras reported by McLean et al. (2020: Fig. 5e), or between their correlative tephras in Lake Suigetsu sediments (SG14-2856/2873 and 2814, respectively: McLean et al., 2020: Fig. 5e). These findings indicate that the trace-element compositions of A-Fm and A-Kn may reflect heterogeneity within these eruptive units. Because we sampled only a single horizon of each of these tephras from the thickest A-Fm and A-Kn units (Supplementary material 4: location 8), on the basis of our data, we cannot address possible vertical variation of shard chemistries within the A-Fm and A-Kn eruptive units. Considering the available shard chemistry data, the trace-element compositions of G5 and G6 shards are very similar to that of A-Fm shards (Supplementary material 1). Their Rb contents (G5, 155 ± 15 ppm; G6, 162 ± 14 ppm; A-Fm, 166 ± 14 ppm, respectively: Supplementary material 2) are linked to their K_2O contents (see above), as indicated by Albert et al. (2019), but the Rb content differences are not large, so cannot be used differentiate among them. Further, the trace-element compositions of spikes G5 and G6 are consistent with those of SG14-2873 shards, but they do not perfectly overlap with the trace-element compositions of A-Fm shards reported by McLean et al. (2020: Fig. 5c and e).

On the other hand, although the trace-element compositions of

Table 3
Matsu'ura.

Spike ID	G1				G3		G4		G5		G6		G6.3		G8.2				G9	
Mode	mode 1		mode 2												mode 1		mode 2			
Horizon ID	2S30-35				9S65-70		9S130-134		10S40-46		10S65-70		11S138-142		16S84-90				16S125-129	
Tephra	K-Ah		Rw AT		AT		A-Kn?		A-Fm		A-Fm		A-Iw		Rw K-Tz?		Aso-4		A-Fk	
(wt.%)	Ave.	1SD	Ave.	1SD	Ave.	1SD	Ave.	1SD	Ave.	1SD	Ave.	1SD	Ave.	1SD	Ave.	1SD	Ave.	1SD	Ave.	1SD
SiO$_2$	74.28	0.69	78.17	0.11	78.09	0.24	78.29	0.20	78.17	0.11	78.16	0.11	77.94	0.14	78.28	0.37	71.56	0.30	78.01	0.26
TiO$_2$	0.60	0.07	0.11	0.06	0.14	0.03	0.14	0.06	0.10	0.05	0.14	0.04	0.16	0.06	0.20	0.08	0.48	0.04	0.18	0.04
Al$_2$O$_3$	13.06	0.22	12.29	0.07	12.33	0.13	12.24	0.12	12.27	0.06	12.29	0.08	12.40	0.08	12.19	0.21	15.17	0.18	12.38	0.12
FeO	2.53	0.19	1.04	0.18	1.17	0.09	1.09	0.09	1.05	0.08	1.08	0.10	1.03	0.07	1.05	0.10	1.65	0.06	1.11	0.09
MnO	0.11	0.05	0.09	0.04	0.05	0.03	0.05	0.05	0.04	0.04	0.06	0.05	0.07	0.04	0.04	0.06	0.12	0.09	0.07	0.04
MgO	0.51	0.06	0.11	0.04	0.13	0.05	0.12	0.03	0.10	0.03	0.12	0.03	0.14	0.04	0.21	0.04	0.46	0.05	0.24	0.04
CaO	2.21	0.33	0.95	0.10	1.14	0.05	1.02	0.06	0.91	0.05	1.07	0.08	1.01	0.05	1.57	0.10	1.60	0.11	1.57	0.08
Na$_2$O	3.77	0.09	3.42	0.13	3.41	0.08	3.33	0.06	3.32	0.04	3.31	0.05	3.48	0.10	3.17	0.05	4.48	0.09	3.18	0.06
K$_2$O	2.92	0.11	3.81	0.12	3.54	0.12	3.72	0.08	4.05	0.08	3.76	0.14	3.77	0.11	3.30	0.06	4.49	0.18	3.25	0.09
Total	100.00		100.00		100.00		100.00		100.00		100.00		100.00		100.00		100.00		100.00	
n	10		5		15		15		15		15		15		9		6		15	
(ppm)	Ave.	1SD	Ave.	1SD	Ave.	1SD	Ave.	1SD	Ave.	1SD	Ave.	1SD	Ave.	1SD	Ave.	1SD	Ave.	1SD	Ave.	1SD
Sc	13.47	1.57	4.97	0.75	5.30	0.89	6.35	0.96	7.75	1.13	8.40	0.96	6.86	0.93	7.45	2.04	7.69	0.77	6.38	0.90
V	13.79	0.85	7.45	1.39	1.42	0.30	1.29	0.13	1.61	0.55	2.36	0.72	3.13	0.29	8.74	1.10	16.81	1.07	7.50	1.02
Cr	1.05	1.05	3.42	1.89	1.72	2.05	0.70	0.61	1.07	1.77	0.30	1.42	-1.59	1.69	1.44	1.29	1.37	1.66	0.68	0.79
Co	1.89	0.12	0.81	0.15	0.46	0.10	0.54	0.10	0.66	0.12	0.57	0.08	0.71	0.09	1.06	0.11	0.88	0.20	0.89	0.13
Ni	1.30	1.56	-0.16	1.18	-0.03	1.45	0.19	0.48	1.13	1.37	0.91	1.13	-0.32	0.96	-0.61	1.13	0.78	1.63	-0.06	0.65
Cu	1.94	0.99	5.37	2.52	1.19	1.08	2.45	0.96	2.91	1.75	1.70	1.09	1.57	1.13	2.60	1.40	4.53	3.40	0.91	0.97
Zn	52.43	1.75	31.36	4.19	13.46	1.55	27.58	2.30	30.83	3.81	37.74	3.85	27.83	2.94	17.68	1.25	45.74	4.05	27.18	1.68
Ga	14.84	0.62	11.21	0.90	9.78	1.02	12.28	1.05	16.14	1.47	17.16	1.53	13.55	1.13	9.54	0.95	17.53	0.65	12.11	1.20
Rb	66	5	134	14	118	13	161	14	155	15	162	14	129	11	92	10	163	12	112	11
Sr	149.7	11.6	64.7	4.4	81.2	8.7	65.6	6.7	56.9	7.4	69.4	6.2	65.7	4.9	87.0	8.6	168.5	12.3	74.6	5.7
Y	40.63	3.08	30.99	2.26	25.66	2.30	24.80	1.96	23.54	3.07	22.96	2.74	20.23	2.09	25.58	3.30	32.88	3.29	10.92	0.57
Zr	266	13	153	14	138	14	119	12	98	9	97	7	102	10	164	17	298	17	109	7
Nb	7.77	0.78	6.97	0.69	7.03	0.81	7.58	0.57	8.55	0.64	8.01	0.58	8.21	0.51	6.26	0.48	16.86	1.52	6.53	0.49
Cs	5.13	0.70	5.90	0.73	6.53	0.56	9.24	0.51	11.12	0.91	11.11	0.76	11.21	0.86	6.56	0.85	8.14	0.53	8.14	0.70
Ba	506	53	449	20	531	31	571	37	595	21	562	21	532	21	497	36	791	34	473	23
La	26.65	3.22	18.01	1.62	27.58	2.82	26.22	2.75	28.14	2.71	27.63	1.81	21.44	1.35	20.02	1.96	34.36	2.80	18.92	1.14
Ce	48.70	5.22	43.30	3.51	44.02	3.29	46.91	2.54	53.60	2.79	54.48	2.44	43.68	2.60	36.08	2.14	70.39	6.68	35.90	1.41
Pr	5.99	0.28	4.32	0.25	4.94	0.44	4.92	0.38	5.79	0.24	5.39	0.27	4.46	0.19	4.85	0.55	8.16	0.95	3.63	0.28
Nd	25.61	2.19	17.31	2.04	20.21	2.12	18.46	1.60	21.19	1.35	19.25	1.65	16.58	1.18	17.11	1.44	32.55	2.06	12.16	1.44
Sm	6.60	0.81	3.66	0.45	4.25	0.30	3.44	0.40	3.67	0.41	3.24	0.46	3.29	0.39	3.83	0.39	6.06	0.31	2.03	0.27
Eu	1.48	0.14	0.61	0.13	0.53	0.08	0.50	0.05	0.41	0.06	0.46	0.09	0.43	0.07	0.69	0.05	1.17	0.18	0.42	0.07
Gd	7.68	0.36	3.46	0.24	4.18	0.44	3.83	0.31	4.57	0.44	3.83	0.28	2.98	0.27	3.20	0.36	7.04	0.39	1.71	0.17
Tb	1.14	0.07	0.54	0.05	0.60	0.08	0.57	0.07	0.65	0.09	0.55	0.07	0.47	0.05	0.57	0.07	0.88	0.08	0.26	0.02
Dy	9.02	0.53	4.28	0.46	4.13	0.46	4.10	0.38	4.38	0.47	4.13	0.35	4.01	0.43	4.24	0.53	6.10	0.59	1.91	0.24
Ho	1.76	0.09	0.91	0.09	0.82	0.08	0.87	0.10	0.94	0.07	0.84	0.07	0.75	0.06	0.94	0.20	1.19	0.13	0.42	0.06
Er	5.05	0.21	3.23	0.33	2.87	0.33	2.76	0.34	2.94	0.22	2.62	0.29	2.39	0.20	3.02	0.63	3.86	0.41	1.41	0.11
Tm	0.75	0.06	0.53	0.05	0.39	0.06	0.39	0.04	0.45	0.06	0.39	0.04	0.36	0.06	0.47	0.10	0.62	0.12	0.26	0.06
Yb	5.21	0.33	3.62	0.30	2.74	0.24	2.79	0.31	3.48	0.38	2.75	0.25	2.85	0.25	3.76	0.52	3.81	0.37	1.57	0.12
Lu	0.76	0.05	0.58	0.09	0.45	0.08	0.44	0.06	0.56	0.10	0.53	0.08	0.36	0.06	0.52	0.10	0.71	0.08	0.32	0.08
Hf	7.48	0.34	4.45	0.62	4.32	0.51	3.89	0.34	3.89	0.37	3.38	0.29	3.72	0.19	5.17	0.60	8.18	0.76	3.74	0.42
Ta	0.55	0.06	0.56	0.06	0.91	0.15	0.93	0.10	1.03	0.12	0.90	0.10	0.94	0.14	0.65	0.08	1.26	0.18	0.75	0.09
Pb	16.16	0.38	22.78	1.57	16.28	1.34	20.26	2.37	27.87	1.85	28.17	1.95	24.67	1.55	18.18	1.66	23.37	1.52	19.53	1.12
Th	8.65	0.91	10.79	0.54	12.74	1.01	12.82	0.89	15.57	0.62	14.15	0.58	12.96	0.54	11.49	1.46	15.26	0.86	11.87	0.50
U	1.73	0.10	2.70	0.19	2.09	0.10	2.42	0.12	3.60	0.14	3.78	0.15	3.33	0.22	2.33	0.21	4.15	0.12	2.63	0.10
n	5		10		14		15		15		15		15		12		7		15	

1SD, 1 standard deviation. FeO* refers to total iron.

Spike ID	G11		G12		G13				G13.1		G14		G15		G16			
Mode					mode 1		mode 2								mode 1		mode 2	
Horizon ID	17S10-15		17S35-37		17S50-55				17S70-75		17S112-114		18S55-60		18S110-115			
Tephra	K-Tz		Aso-ABCD?		Ata		Aso		UT-9.10		Aso-3iii		Kuju		Aso-3ii		Aso-3ii	
(wt.%)	Ave.	1SD	Ave.	1SD	Ave.	1SD	Ave.	1SD	Ave.	1SD	Ave.	1SD	Ave.	1SD	Ave.	1SD	Ave.	1SD
SiO$_2$	78.51	0.22	70.63	0.26	74.75	0.37	71.30	0.12	73.85	0.18	69.55	0.43	77.43	0.45	70.95	0.35	62.41	0.86
TiO$_2$	0.24	0.06	0.62	0.05	0.48	0.14	0.58	0.03	0.62	0.06	0.73	0.06	0.18	0.06	0.62	0.08	0.97	0.07
Al$_2$O$_3$	11.86	0.10	14.98	0.10	13.22	0.11	14.79	0.08	13.36	0.06	15.28	0.18	12.65	0.12	14.92	0.15	16.26	0.26
FeO	1.07	0.08	2.29	0.12	2.06	0.18	2.03	0.04	2.48	0.13	2.56	0.14	0.93	0.18	2.12	0.14	5.95	0.45
MnO	0.07	0.05	0.16	0.08	0.08	0.08	0.17	0.04	0.10	0.05	0.13	0.05	0.11	0.06	0.05	0.05	0.25	0.13
MgO	0.19	0.05	0.59	0.04	0.54	0.05	0.47	0.02	0.57	0.05	0.72	0.07	0.22	0.03	0.48	0.04	2.16	0.22
CaO	1.10	0.04	1.69	0.09	2.02	0.16	1.41	0.03	2.29	0.07	1.98	0.21	1.32	0.17	1.57	0.12	4.84	0.23
Na$_2$O	3.49	0.05	4.23	0.06	3.89	0.07	4.22	0.07	3.80	0.05	4.10	0.06	3.17	0.06	4.09	0.07	3.78	0.12

Table 3 (*continued*)

																		mode 2.1	mode 2.2
K₂O	3.47	0.04	4.81	0.05	2.96	0.09	5.02	0.07	2.92	0.07	4.97	0.14	4.00	0.11	5.19	0.07	3.41	0.19	
Total	100.00		100.00		100.00		100.00		100.00		100.00		100.00		100.00		100.00			
n	15		15		8		3		12		15		13		7		4			

(ppm)	Ave.	1SD	Ave.	1SD	Ave.	1SD	Ave.	1SD	Ave.	1SD	Ave.	1SD	Ave.	1SD	Ave.	1SD	Ave. (mode 2.1)	1SD	Ave. (mode 2.2)	1SD
Sc	7.48	1.04	14.71	2.17	14.82	0.93	9.72	2.89	15.63	2.02	13.95	2.79	2.21	0.66	12.74	1.40	18.42	1.45	15.06	1.62
V	10.92	1.47	35.26	5.05	15.01	0.80	12.01	1.89	25.54	2.86	27.00	2.47	7.99	0.93	12.95	1.46	41.11	8.87	144.00	10.49
Cr	1.72	2.14	-0.04	0.75	-0.48	0.47	0.47	1.26	1.18	1.15	0.75	1.40	0.95	1.53	0.58	0.71	4.64	1.11	0.88	0.99
Co	0.96	0.20	1.90	0.30	1.21	0.19	0.61	0.30	2.05	0.29	1.91	0.22	1.02	0.17	3.39	0.95				
Ni	-1.76	2.95	2.31	1.61	1.02	0.71	0.67	1.57	1.78	1.69	1.91	1.77	0.42	2.11	-0.54	1.68	-1.25	0.97	-1.03	1.80
Cu	4.03	1.16	10.18	5.11	1.85	0.86	2.69	2.22	2.29	1.48	3.49	1.11	1.78	1.23	2.19	0.72	9.98	2.03	24.18	7.26
Zn	25.89	1.93	38.51	5.17	50.10	4.92	34.59	16.08	50.32	5.05	30.47	3.39	24.60	2.35	35.13	2.75	68.33	6.82	45.18	5.39
Ga	11.42	0.80	12.67	1.32	15.09	1.40	16.34	4.97	14.94	1.53	15.24	2.01	12.49	1.30	16.41	1.93	17.84	0.22	16.85	0.51
Rb	92	5	114	12	79	8	168	36	79	6	134	12	99	7	159	17	112	4	87	3
Sr	60.5	4.6	240.7	24.7	128.4	8.7	87.8	13.4	152.5	12.7	262.3	28.1	170.6	15.2	232.0	14.0	453.5	23.2	486.9	57.0
Y	31.24	2.47	47.46	4.73	45.47	2.94	35.33	6.67	47.70	3.99	36.10	2.69	6.82	0.56	41.41	2.50	31.22	2.24	34.16	1.36
Zr	171	10	340	32	218	28	321	28	241	14	309	23	90	6	359	21	317	28	241	14
Nb	5.85	0.46	14.41	1.35	10.62	0.71	18.88	2.57	11.95	1.37	18.07	1.49	11.50	0.83	20.46	0.92	14.89	0.49	13.55	1.09
Cs	4.58	0.30	6.31	0.76	3.72	0.42	11.81	1.47	4.45	0.46	9.92	0.76	5.39	0.39	11.36	1.12	5.20	0.90	6.06	0.53
Ba	417	20	743	67	417	29	715	67	439	23	795	53	847	41	828	39	648	14	670	43
La	18.45	1.60	35.30	3.28	24.89	1.48	31.44	4.79	27.10	1.63	37.20	2.69	22.98	1.83	37.64	2.51	35.22	2.72	33.57	0.65
Ce	31.44	2.00	64.06	7.12	48.93	3.48	72.80	5.76	55.36	4.34	72.60	5.65	38.85	2.74	74.28	3.67	61.38	2.63	63.91	4.40
Pr	4.20	0.27	8.74	0.86	6.41	0.33	8.65	0.63	7.17	0.53	9.16	0.67	3.61	0.25	9.67	0.55	9.29	0.87	9.36	0.65
Nd	17.71	1.19	36.96	3.75	27.68	1.89	34.46	3.35	29.81	2.63	38.78	3.25	13.11	1.83	40.67	2.36	34.38	1.99	40.87	2.19
Sm	4.29	0.47	8.40	0.81	6.19	0.60	7.20	0.85	7.13	0.56	8.27	0.98	1.75	0.25	7.63	0.82	9.06	0.73	8.50	0.76
Eu	0.54	0.06	1.49	0.16	1.16	0.18	1.08	0.17	1.57	0.14	1.66	0.20	0.44	0.10	1.70	0.16	1.80	0.24	1.70	0.04
Gd	4.62	0.29	7.86	0.94	6.89	0.72	6.06	0.43	8.60	1.00	8.10	0.77	1.37	0.19	8.09	0.38	7.46	0.61	7.16	0.35
Tb	0.74	0.07	1.08	0.08	1.07	0.12	0.80	0.07	1.29	0.18	1.20	0.17	0.21	0.05	0.94	0.08	0.94	0.11	0.89	0.08
Dy	5.53	0.45	6.99	0.65	7.88	0.94	5.77	0.72	8.24	0.91	7.16	0.77	1.29	0.14	6.67	0.38	5.29	0.62	6.26	0.34
Ho	1.27	0.15	1.49	0.15	1.62	0.18	1.31	0.17	1.76	0.19	1.52	0.17	0.21	0.04	1.51	0.11	1.07	0.02	1.02	0.12
Er	3.83	0.26	3.52	0.28	5.87	0.43	3.84	0.36	5.71	0.56	4.59	0.57	0.79	0.08	4.27	0.24	3.52	0.18	3.58	0.19
Tm	0.64	0.05	0.65	0.08	0.85	0.08	0.63	0.09	0.90	0.09	0.72	0.10	0.11	0.02	0.75	0.07	0.43	0.02	0.46	0.05
Yb	4.47	0.41	4.63	0.30	5.54	0.26	4.09	0.52	5.55	0.45	4.94	0.49	1.14	0.17	4.45	0.29	3.07	0.07	3.22	0.19
Lu	0.81	0.11	0.72	0.05	0.88	0.11	0.61	0.08	0.89	0.10	0.72	0.09	0.22	0.05	0.66	0.05	0.56	0.04	0.44	0.09
Hf	5.68	0.55	8.97	0.48	7.28	0.43	9.56	1.08	6.71	0.49	8.86	0.58	2.98	0.28	9.08	0.30	6.74	0.22	6.12	0.49
Ta	0.48	0.12	1.32	0.13	0.69	0.09	1.30	0.31	0.84	0.12	1.49	0.13	0.98	0.19	1.68	0.17	0.85	0.05	1.15	0.11
Pb	21.06	1.41	19.66	2.60	20.99	1.26	25.46	5.01	19.86	1.90	21.02	1.88	17.22	1.61	21.80	1.76	18.69	2.30	12.40	0.58
Th	10.74	0.98	17.13	0.73	10.25	0.58	18.64	1.78	9.75	0.53	16.48	1.22	11.13	0.58	18.33	0.59	11.42	0.42	11.43	0.52
U	2.44	0.15	3.86	0.33	2.18	0.12	5.26	1.04	1.97	0.14	3.84	0.32	2.35	0.18	4.24	0.29	3.04	0.15	2.54	0.11
N	13		14		8		7		13		15		15		15		3		4	

	G17		G18				G21		G22		G22.1		G22.2		G24	
Spike ID	G17		G18				G21		G22		G22.1		G22.2		G24	
Mode			mode 1		mode 2											
Horizon ID	19S50-55		20S0-6.5				25S34-38		26S70-75		27S45-51.5		28S5-10		30S130-135	
Tephra	Aso-3i		Aso-2				Ata-Th		Aso		Rw Tky-Ng1		Tky-Ng1		Kkt	
(wt.%)	Ave.	1SD	Ave.	1SD	Ave.	1SD	Ave.	1SD	Ave.	1SD	Ave.	1SD	Ave.	1SD	Ave.	1SD
SiO₂	69.69	0.46	59.81	0.61	68.53	0.98	78.14	0.20	70.97	0.22	77.93	0.13	77.98	0.21	76.66	0.18
TiO₂	0.78	0.06	1.21	0.07	0.65	0.02	0.15	0.06	0.55	0.06	0.13	0.05	0.15	0.07	0.21	0.05
Al₂O₃	15.09	0.22	16.15	0.29	15.26	0.19	12.43	0.13	15.08	0.12	12.04	0.09	11.98	0.14	12.64	0.09
FeO	2.62	0.14	7.61	0.31	3.49	0.80	1.00	0.12	1.99	0.13	0.86	0.06	0.95	0.14	1.26	0.09
MnO	0.12	0.09	0.14	0.06	0.09	0.05	0.09	0.06	0.12	0.06	0.08	0.09	0.06	0.06	0.11	0.08
MgO	0.70	0.08	2.66	0.23	0.71	0.03	0.19	0.03	0.53	0.07	0.12	0.04	0.09	0.04	0.13	0.02
CaO	1.93	0.18	5.60	0.36	2.25	0.07	1.27	0.06	1.85	0.10	0.94	0.05	0.92	0.09	0.98	0.05
Na₂O	4.03	0.09	3.46	0.13	3.80	0.02	3.54	0.18	3.93	0.07	2.69	0.06	2.66	0.06	3.55	0.05
K₂O	5.04	0.16	3.38	0.22	5.23	0.00	3.20	0.16	4.99	0.09	5.21	0.11	5.22	0.10	4.45	0.08
Total	100.00		100.00		100.00		100.00		100.00		100.00		100.00		100.00	
N	15		13		2		15		15		13		14		15	
(ppm)	Ave.	1SD	Ave.	1SD	Ave.	1SD	Ave.	1SD	Ave.	1SD	Ave.	1SD	Ave.	1SD	Ave.	1SD
Sc	13.35	2.06	25.23	2.44	-	-	3.31	0.85	9.18	1.24	-	-	2.16	0.61	10.85	1.37
V	23.49	2.10	226.57	43.12	-	-	2.76	0.51	28.81	2.05	-	-	2.63	0.67	2.60	0.28
Cr	1.06	0.36	1.01	0.97	-	-	0.18	1.09	0.05	0.84	-	-	0.87	1.02	2.41	1.72
Co	1.41	0.14	19.56	3.70	-	-	0.78	0.15	1.87	0.16	-	-	0.50	0.13	0.60	0.11
Ni	0.21	1.06	5.07	4.44	-	-	0.52	1.82	1.08	0.95	-	-	0.50	1.00	-0.87	1.82
Cu	1.55	0.45	158.95	48.94	-	-	1.40	1.02	2.44	0.56	-	-	2.72	0.87	3.51	0.86
Zn	37.16	3.52	75.43	32.35	-	-	27.12	2.07	27.88	2.86	-	-	20.46	5.00	34.55	4.54
Ga	19.03	1.47	20.50	3.45	-	-	13.09	1.80	15.35	1.13	-	-	12.41	0.72	14.88	0.89
Rb	121	11	91	14	-	-	105	10	133	13	-	-	164	7	155	10
Sr	236.1	22.6	485.6	24.0	-	-	78.3	8.0	241.4	25.1	-	-	97.6	5.4	78.2	4.3
Y	32.06	2.80	31.14	1.43	-	-	17.43	2.68	28.20	1.79	-	-	13.64	1.19	34.96	1.44
Zr	278	21	201	9	-	-	93	10	303	18	-	-	103	9	192	12

Table 3 (*continued*)

Nb	15.25	1.25	12.22	0.86	-	-	7.31	0.66	15.26	1.01	-	-	7.44	0.87	8.81	0.51
Cs	8.91	0.88	6.16	0.99	-	-	6.78	0.66	8.92	0.57	-	-	7.94	0.71	10.99	0.62
Ba	727	47	638	27	-	-	462	29	690	47	-	-	567	44	582	23
La	33.39	2.24	29.83	2.26	-	-	24.87	2.69	33.12	2.23	-	-	32.02	3.56	29.40	1.43
Ce	70.70	4.78	62.54	4.03	-	-	42.49	3.71	60.98	3.96	-	-	47.21	4.88	63.34	3.12
Pr	9.05	0.62	8.36	0.42	-	-	4.76	0.43	7.58	0.36	-	-	4.73	0.49	7.29	0.39
Nd	38.48	1.93	34.64	2.44	-	-	17.22	1.36	31.42	1.57	-	-	16.33	1.63	29.31	0.93
Sm	8.75	0.64	8.20	0.75	-	-	2.51	0.46	5.33	0.56	-	-	2.04	0.28	6.52	0.39
Eu	1.71	0.12	2.01	0.15	-	-	0.44	0.07	1.27	0.12	-	-	0.38	0.07	0.76	0.07
Gd	7.36	0.79	6.55	0.75	-	-	2.77	0.30	5.36	0.33	-	-	1.98	0.17	5.83	0.27
Tb	0.98	0.08	0.84	0.12	-	-	0.43	0.06	0.82	0.05	-	-	0.32	0.08	1.00	0.07
Dy	6.60	0.45	5.79	0.77	-	-	2.84	0.26	4.84	0.33	-	-	2.16	0.23	6.16	0.24
Ho	1.31	0.11	1.13	0.21	-	-	0.56	0.05	1.08	0.10	-	-	0.49	0.07	1.39	0.08
Er	4.41	0.28	3.65	0.36	-	-	1.93	0.24	3.03	0.29	-	-	1.30	0.12	4.10	0.20
Tm	0.60	0.06	0.47	0.04	-	-	0.31	0.04	0.51	0.05	-	-	0.24	0.03	0.54	0.03
Yb	4.26	0.27	3.34	0.44	-	-	2.22	0.17	3.14	0.22	-	-	1.97	0.17	3.99	0.24
Lu	0.68	0.06	0.46	0.05	-	-	0.42	0.04	0.53	0.04	-	-	0.28	0.03	0.65	0.07
Hf	8.59	0.45	5.43	0.56	-	-	3.63	0.32	7.86	0.44	-	-	3.50	0.25	6.08	0.25
Ta	1.48	0.12	1.03	0.12	-	-	0.76	0.10	1.45	0.10	-	-	1.13	0.10	0.80	0.09
Pb	23.91	1.45	15.90	2.09	-	-	15.95	1.21	18.76	0.98	-	-	17.97	1.49	32.50	1.59
Th	18.28	0.83	10.62	0.81	-	-	11.61	0.69	15.75	0.65	-	-	23.59	1.07	14.69	0.60
U	4.62	0.23	3.00	0.41	-	-	2.00	0.10	3.46	0.15	-	-	3.84	0.23	3.55	0.13
n	13		15				15		13				14		15	

spike G4 and A-Kn shards are roughly similar, their Th content ranges (Fig. 5c) and other trace-element content ranges (e.g., V, Co, Nb, Pr, Nd, Gd, and Ho: Supplementary material 1) showed subtle differences. Further, the compositions of the shards did not well overlap with those of SG14-2814 and A-Kn reported by McLean et al. (2020: Fig. 5c and e).

Therefore, we first correlated one of G5 or G6 with A-Fm on the basis of the similarities of their shard chemical compositions. This tephra correlation is supported by the similar tephrostratigraphy between cores MD012422 and SG14, namely, the paired occurrence of similar tephras at closely spaced stratigraphic positions (G5 and G6 in core MD012422 and SG14-2856 and −2873 in core SG-14 (McLean et al., 2020). The spike G5 and G6 horizons are 1−1.5 m deeper than the reported A-Fm horizon of 12.76−12.78 mbsf (Ikehara et al., 2006), but we re-correlated the reported A-Fm to AT on the basis of glass shard morphology and shard chemistry (see section 5.1.2). Therefore, we suggest that spike G4 is an Aira caldera-originated tephra, which, considering its stratigraphic relationship with the underlying A-Fm tephra in the proximal area and in Lake Suigetsu, may correspond to the A-Kn eruption.

5.1.4. Subspike G6.3 and Aira-Iwato tephra

Subspike G6.3 (16.40−16.44 mbsf) included a large amount of poorly vesiculated L-type shards and minor amounts of H-type and M-type shards, and we observed sand patches in this horizon but no visible tephra layer (Table 2). The glass shards are similar to those of tephras from Aira caldera, except A-Fk, with respect to their SiO2 and K2O content ranges (Fig. 5a) and their FeO*, CaO, Na2O, and Al2O3 content ranges (Supplementary material 5). Both Albert et al. (2019) and McLean et al. (2020) differentiated A-Iw and AT by their Th and Zr content ranges, but in our samples, the Th and Zr content ranges of these tephras, though close to the reported ranges, partly overlap (Fig. 5b); therefore, it is difficult for us to differentiate A-Iw and AT on this basis. Further, A-Iw and AT shards are similar in their U contents (Fig. 5d and f). Subspike G6.3 includes a moderate number of H-type shards, similar to A-Os and A-Iw, both of which include large numbers of moderately and poorly vesiculated shards (M- and L-types) and a small number of highly vesiculated shards (H-type) (Supplementary material 7); therefore, the subspike may correlate with A-Os or A-Iw. However, because A-Os is the lowest AT eruption unit (Machida and Arai, 2003) and no spike or subspike below spike G3 (AT) can be correlated with A-Os,

we correlate subspike G6.3 with A-Iw on the basis of shard morphology. In addition, subspike G6.2 is positioned above subspike G6.3, and its shards are similar to those of G6.3 (Fig. 5a), indicating that they were reworked from the subspike G6.3 horizon. The subspike G6.3 horizon is slightly (ca. 0.4 m) deeper than the reported A-Iw horizon depth of 16.02−16.04 mbsf (Ikehara et al., 2006).

5.2. MIS 5 (70−130 ka)

5.2.1. Subspike G8.2 and Aso-4 tephra

Subspike G8.2 (23.35−23.41 mbsf) included many H-type and M-type shards with minor amounts of L-type shards, and we observed sandy silt but no visible tephra layer in this horizon (Table 2). The subspike shards had bimodal chemical compositions: modes 1 (higher SiO2) and 2 (lower SiO2) are similar to the A-Fk/K-Tz and Aso-4 compositional fields, respectively (Table 3; Fig. 6a). The Th, Zr, Y, and V contents of subspike G8.2 modes 1 and 2 are also similar to those of K-Tz and Aso-4, respectively (Fig. 6b−d). Because subspike G8.2 is positioned above spike G11 (K-Tz, see section 5.2.3), the G8.2 horizon probably includes secondary deposition of K-Tz shards. Aso-4 grains were not detected in core MD012422 by Ikehara et al. (2006); therefore, we interpreted G8.2, the lowest subspike including a few Aso-4 shards stratigraphically positioned above A-Fk (see Section 5.2.2), as the Aso-4 horizon. This study is the first to report an Aso-4 horizon in the core. This Aso-4 horizon (MIS 5b) indicates that the length, 6.44−6.50 m, of the segment extending from MIS 5b (23.35−23.41 mbsf) to the MIS 4/5 boundary (16.91 mbsf: Ikehara et al., 2006) (Fig. 2), is probably overestimated; therefore, the age model for this segment should be reconsidered (see Section 6.1).

5.2.2. Spike G9 and Aira-Fukuyama tephra

Spike G9 (23.71−23.95 mbsf) included a large amount of M-type shards with minor amounts of H-type and L-type shards (Table 2). It also included a large amount of amphibole grains. We observed a visible light gray to yellowish gray tephra layer in this horizon (Table 2). The glass shards are similar to A-Fk mode 1 with respect to their SiO2, K2O, Th, Zr, Y, and V content ranges (Fig. 6a−d). Unlike A-Fk, however, the spike G9 shards were not bimodal in their chemical composition. The Y contents of spike G9 and of A-Fk mode 1 (Fig. 6d) are very low (10.92 ± 0.57 and 11.49 ± 1.76 ppm,
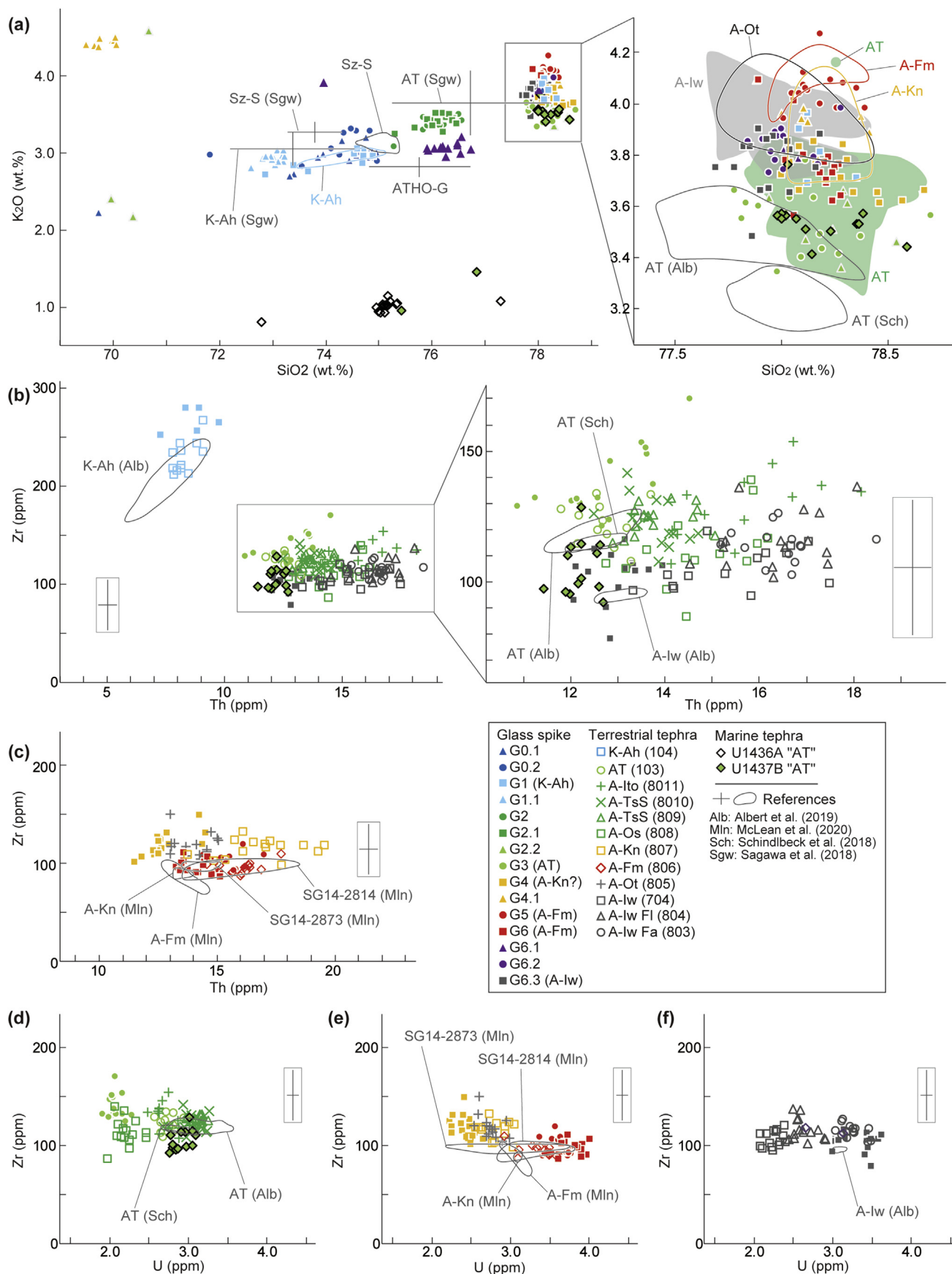
Fig. 5. Chemical compositions of glass shards from tephras corresponding to MIS 1 to 4. (a) SiO_2 versus K_2O; (b), (c) Th versus Zr; (d), (e), and (f) U versus Zr. The ranges of terrestrial tephras are encircled. Information on the sampled terrestrial tephras is in Table 1. The shard major-element compositions of Schindlbeck et al. (2018) and Albert et al. (2019),

respectively: Table 3 and Supplementary 2), close to the Y contents of tephras from Kuju, Sambe, and Daisen volcanoes (Fig. 4b; Albert et al., 2019) and quite different from the Y contents of any other tephras from Kyushu Island. However, the Ba content ranges of spike G9 and A-Fk shards (473 ± 23 and 421 ± 12 ppm, respectively: Table 3 and Supplementary 2) are lower than those of the Kuju tephra series (see section 4.2). The trace-element compositions of spike G9 and A-Fk mode 1 showed subtle differences in their Ba, Zn, Ga, Nb, Pb, and U contents (Supplementary material 1), indicating heterogeneity of the original magma or the existence of two closely spaced eruptive units, as with other Aira caldera-derived tephras (sections 5.1.2−5.1.4). Although the trace-element composition of spike G9 does not perfectly overlap with that of A-Fk, no other possible correlatives of A-Fk have been reported. Therefore, we tentatively correlate spike G9 with A-Fk. The spike G9 horizon corresponds to the reported A-Fk horizon of 23.81−23.89 mbsf (Ikehara et al., 2006).

5.2.3. Spike G11 and Kikai-Tozurahara tephra

Spike G11 (24.10−24.15 mbsf) included a large amount of H-type shards with a minor amount of M-type shards, but we did not observe a corresponding visible tephra in our core examination. Most shards are similar to those of the K-Tz shards from Kikai caldera with respect to their SiO_2, K_2O, Th, Zr, and Y content ranges (Fig. 6a, b, 6d). However, the Ba and Ce contents of spike G11 (374−443 and 28.4−34.6 ppm, respectively) are lower than those of K-Tz (437−522 and 38.8−46.4 ppm, respectively) (Supplementary material 1). Reported data of K-Tz shards display a similar compositional variation: shards with lower Ba and Ce, similar to G11 shards, were reported by Kimura et al. (2015: 416 ± 3 and 35.0 ± 0.99 ppm, respectively) and by Maruyama et al. (2017: 417 ± 26 and 36.8 ± 1.8 ppm, respectively), whereas shards with higher Ba and Ce, similar to our K-Tz sample, were reported by Albert et al. (2019: 476−561 and 37.3−48.1 ppm, respectively) and by Maruyama et al. (2020: 483 ± 37 and 40.3 ± 2.6 ppm, respectively). These variations in Ba and Ce contents probably correspond to a compositional array with a positive slope, because the Ce/Ba ratio of each sample is similar. In light of this, we interpreted spike G11 and the K-Tz shards of this study as plotting in the lower and higher Ba and Ce fields in the array, respectively. Therefore, we correlate spike G11 with K-Tz; the K-Tz horizon was first detected in core MD012422 by this study. K-Tz has been dated to MIS 5c−5b (Machida and Arai., 2003), which leads us to reconsider the age model of MIS 5b−5a (see Section 6.1). We assigned the age as 94.5 ± 4.8 ka with reference to the reported K-Tz (Albert et al., 2019).

5.2.4. Spike G12 and the Aso-ABCD tephra

Spike G12 (24.35−24.37 mbsf) included a large amount of M-type shards with minor amounts of H-type shards, and we observed a sand patch but no tephra layer in this horizon (Table 2). Most shards are similar to Aso-A, -B, −C, and -D shards from terrestrial deposits on Shikoku Island with respect to their SiO_2 and K_2O content ranges (Fig. 6a). Further, on the bi-plot of Th and Zr (Fig. 6c), the compositional array of G12 shards is consistent with the arrays of Aso-A, -B, −C, and -D (mode 1). Although Albert et al. (2019) suggested that Aso-A and -D, which include higher Th and Zr shards, are distinguishable from Aso-B and −C, which include lower Th and Zr shards, when considered together, these four units (excluding Aso-D mode 2) appear to form a single systematic

compositional array in the results of both this study and Albert et al. (2019). Therefore, we suggest that spike G12 correlates to Aso-ABCD, but we cannot confidently correlate it with any one of Aso-A, -B, −C, or -D. The Aso-ABCD array occurs between K-Tz and Ata (Machida and Arai, 2003); therefore, we assigned the age as 89.7−105.3 ka with reference to the reported K-Tz and Ata ages (Albert et al., 2019).

5.2.5. Spike G13 and subspike G13.1 and the Ata and UT-9.10 tephras

Spike G13 and subspike G13.1 (24.50−24.55 and 24.65−24.86 mbsf, respectively) included a large amount of M-type shards, but we observed no visible tephra layers in these horizons (Table 2). Both spike G13 and subspike G13.1 include Aso- and Ata caldera-derived tephra shards with high and moderate K_2O content, respectively (Fig. 6a). Further, their shards are also similar to those of the UT-9.10 tephra of Tsuji et al. (2018: 8 of 15 shards: SiO_2, 73.4−74.2 wt%, and K_2O, 2.8−3.0 wt%) from terrestrial deposits in core UT from Shikoku Island. The remaining UT-9.10 shards (7 of 15 shards) had two additional populations (SiO_2, 73.6−77.8 and 75.8−79.3 wt%, and K_2O, 5.5 and 2.9−3.9 wt%, respectively) (Tsuji et al., 2018). The UT-9.10 tephra is positioned below Ata in the UT core and has been correlated to the BT38 tephra in the Takashima-oki core (Fig. 1b; Tsuji et al., 2018). However, the ages of the UT-9.10 (108.8 ka; Tsuji et al., 2018) and BT38 (130.7 ka; Nagahashi et al., 2007) tephras are different and thus do not support this correlation (see section 6).

The G13 shards had bimodal chemical compositions: mode 1, low Th and low Zr; mode 2, high Th and high Zr (Fig. 6b). The Th and Zr content ranges of mode 1 are similar to those of Ata, and those of mode 2 are similar to the content ranges in terrestrial Aso-4 (sample 1301) and Aso-ABCD (Fig. 6b and c). Because G13 is stratigraphically below G8.2 (Aso-4), G9 (A-Fk), and G11 (K-Tz), G13 cannot correlate to Aso-4. Further, G13 shards are different from Aso-ABCD shards with respect to their V, Rb, Sr, Co, Nb, Cs, Rb, and U contents (Supplementary material 1). Therefore, we suggest that G13 modes 1 and 2 correspond to Ata and an Aso caldera-derived tephra, respectively.

The G13.1 shards are characterized by low Th, similar to Ata shards (Fig. 6b−d). However, 13 of 15 shards in subspike G13.1 had high Co and high V contents (>1.5 and > 19.6 ppm, respectively), unlike the terrestrial Ata shards (Co, <1.7 ppm; V, <17.1 ppm) and the shards in spike G13 (Co, <1.5 ppm; V, <16.3 ppm) (Fig. 6e). Therefore, subspike G13.1 corresponds to a tephra that includes pre-Ata shards (i.e., an unnamed Ata volcano-originated tephra) (Fig. 2). In a future study, the trace-element composition of UT-9.10 shards should be obtained and the possible correlation of G13.1 to the UT-9.10 tephra should be examined.

5.3. MIS 5 to 6 (130−190 ka)

5.3.1. Spikes G14, G16, and G17 and the Aso-3 tephra

Spikes G14, G16, and G17 (25.11−25.15, 26.60−26.65, and 27.50−27.55 mbsf, respectively) included large amounts of M-type shards with minor amounts of H-type and L-type vesiculated shards. Among these spikes, the G16 shards are the most vesiculated, as shown by their H- and M-type shard composition (Table 2). We observed sand patches in the G14 horizon and sandy silt in the G16 and G17 horizons but no visible tephra layers in any of these horizons (Table 2). The shards in spikes G14 and G17 were

---

obtained by wavelength-dispersive (WDS) EPMA, were recalculated by the authors to compare with our EDS-EPMA data, and the recalculated ranges are encircled. The shard major-element compositions (average and 1 SD) of Sagawa et al. (2018) obtained by EDS-EPMA are displayed as crosses. The trace-element compositions of Schindlbeck et al. (2018) and Albert et al. (2019) obtained by LA-ICP-MS are also encircled. Error bars on plots represent reproducibility, calculated as 2 SD of replicate analyses of MPI-DING ATHO-G. Outliers not plotted are included in Supplementary material 1. Bi-plots of SiO_2 versus alkali, FeO* versus CaO, and Na_2O versus Al_2O_3 are in Supplementary material 5a−c.

Fig. 6. Chemical compositions of glass shards from tephras corresponding to MIS 5. (a) SiO_2 versus K_2O; (b), (c) Th versus Zr; (d) Th versus Y; and (e) Co versus V. The ranges of terrestrial tephras are encircled. Information on the sampled terrestrial tephras is in Table 1. The shard major-element compositions of Schindlbeck et al. (2018) and Albert et al.

unimodal with respect to their SiO_2 and K_2O contents (SiO_2, >68 wt % and K_2O, >4.8 wt%), whereas the shards in spike G16 had bimodal ranges: mode 1, lower SiO_2 and K_2O; mode 2, higher SiO_2 and K_2O (Table 3). The two modes of spike G16 form an array with a positive slope on the SiO_2−K_2O bi-plot (Fig. 7a). Modes 1 and 2 correspond to lower and higher Sr, Co, and V content ranges, respectively (Table 3; Fig. 7d and e); therefore, the G16 shards are chemically similar to terrestrial Aso-3 shards from location 6 (sample 601; Table 1). In particular, the presence of lower SiO_2 and higher Sr shards in G16 indicates that G16 probably corresponds to an upper Aso-3 ignimbrite (Aso-3B or Aso-3C), and not to the basal fall (Aso-3W) or the lowermost Aso-3 ignimbrite (Aso-3A) (Albert et al., 2019). Further, because SiO_2 and K_2O of the proximal Aso-3A shards (sample 202) are unimodally distributed, Aso-3A is potentially correlated to spike G17, below G16 (Aso-3B or Aso-3C). However, the Co and V contents of Aso-3A shards are low, unlike those of spike G17 shards (Fig. 7e); thus, spike G17 is not correlated to Aso-3A. We therefore designated spikes G14, G16, and G17 as Aso-3iii, Aso-3ii, and Aso-3i, respectively (Fig. 2).

A distal Aso-3 deposit, BT39, in the Takashima-oki core in central Japan (Fig. 1b), is a unique tephra in that it contains glass shards with bimodal SiO_2 and K_2O distributions and the compositional array has a positive slope (Nagahashi et al., 2004). The compositional array of BT39 and its correlative (Aso-3) shards (Nagahashi et al., 2004) is similar to that spike G16 in this study (Fig. 7a); therefore, BT39 is correlated to spike G16 and to terrestrial Aso-3 (sample 601). BT39 has been dated to 132.1 ka, based on the sedimentation rate chronology of lacustrine (Lake Biwa) sediments; this age is consistent with the age of spike G16 in the $\delta^{18}O$ stratigraphy of core MD012422 (transition from MIS 6 to 5; Fig. 2). Further, BT40, 41, and 42, just below BT39 in the Takashima-oki core, contain Aso-3 shards with unimodal SiO_2 and K_2O distributions that have been dated to 132.7, 133.0, and 143.6 ka, respectively (Nagahashi et al., 2004, 2015). BT40 and 41 have been correlated to pre-BT39 units in an intermittent Aso-3 eruptive sequence (Nagahashi et al., 2004). However, BT42 is much older than the BT39−41 series; therefore, BT42 may correlate to spike G17 (Aso-3i), the age of which corresponds to the MIS 6 maximum (133−140 ka; Bassinot et al., 1994; Lisiecki and Raymo, 2005).

Aso-3 tephra has been found in deep-sea cores at some locations in the Japan Sea, and its age was determined to be 133.3 ka, transition from MIS 6 to 5, by lithostratigraphy (Chun et al., 2004). Because Chun et al. (2004) reported major-element data from only three shards, we could not confidently judge whether their shards belong to a unimodal or multimodal population; thus, we do not assign their Aso-3 to either Aso-3ii or Aso-3i. The UT-9.87 tephra in core UT from Shikoku Island (Fig. 1b) has been correlated to Aso-3 on the basis of the major-element composition of its shards, and its age was determined to be 112.7 ka from the sedimentation rate chronology of terrestrial basin sediments (Tsuji et al., 2018). This age is consistent with that of Aso-3iii (MIS 5c−5e); however, because the UT-9.87 age is based on the sedimentation rate of the basin sediments, which was not constant within the MIS 5 segment, the estimated age would vary, depending on the sedimentation rate used. Therefore, although we suggest that UT-9.87 and Aso-3iii may be correlated, we do not assign the UT-9.87 age to Aso-3iii. The UT-9.87 tephra in core UT from Shikoku Island (Fig. 1b) has been correlated to Aso-3 on the basis of the major-element composition of its shards, and its age was determined to be 112.7 ka from the sedimentation rate chronology of terrestrial

basin sediments (Tsuji et al., 2018). This age is consistent with that of Aso-3iii (MIS 5e). However, because as indicated above the UT-9.87 age is based on the sedimentation rate of the basin sediments, which varied within the MIS 5 segment, the estimated age of this tephra depends on the sedimentation rate used. Therefore, although we suggest that UT-9.87 and Aso-3iii may be correlated, we do not assign the UT-9.87 age to Aso-3iii.

5.3.2. Spike G15 and a Kuju-volcano derived tephra

Spike G15 (26.50−26.10 mbsf) included a large amount of L-type shards as well as a large amount of amphibole grains, but we did not observe any visible tephra layer in this horizon (Table 2). Most shards are similar to Kj-m rather than to Kj-Sm with respect to their K_2O contents (Fig. 7a). However, with respect to their Y and Sr contents (expressed as Sr/Y: Fig. 7f), the shards are similar to Kj-Sm rather than to Kj-m. Other major- and trace-element compositions of Kj-Sm and Kj-m, including those for Kj-m reported by Albert et al. (2019), are not discriminative; therefore, we cannot correlate spike G15 to Kj-Sm or Kj-m on the basis of glass shard chemistry.

In central Kyushu, Aso-3 occurs stratigraphically between Kj-Sm and Kj-m; that is, Kj-Sm is positioned between Aso-4 and Aso-3, and Kj-m is between Aso-3 and Aso-2 (Ono et al., 1977). However, the occurrences of Aso-3i, Aso-3ii, and Aso-3iii in core MD012422 determined by this study indicate that the stratigraphy of the proximal Aso-3 series is probably rather more complicated than we realized previously. Therefore, we cannot confidently attribute Kj-Sm, Kj-m, or an unreported Kuju tephra as correlative of spike G15.

5.3.3. Spike G18 and Aso-2 tephra

Spike G18 (28.50−28.57 mbsf) included a large amount of L-type shards, and we observed coarse black sand but no visible tephra layer in this horizon (Table 2). With respect to their SiO_2 and K_2O content ranges, most shards are very similar to the UT-14.55 tephra shards, which Tsuji et al. (2018) inferred to correlate to Aso-2, in core UT from Shikoku Island (Tsuji et al., 2018: Fig. 7a). However, the SiO_2 and K_2O ranges of these spike G18 and UT-14.55 shards are slightly lower than those of our terrestrial Aso-2 sample (Fig. 7a). The shards of spike G18, the UT-14.55 tephra, and Aso-2 are distributed along a compositional array with a positive slope and an intercept higher on the K_2O axis than that of the Aso-3 and Aso-4 shard arrays (Nagahashi et al., 2004: Fig. 7a). Spike G18, UT-14.55, and Aso-2 shards are similar with respect to their FeO*, CaO, and Al_2O_3 content ranges, although the Na_2O contents of spike G18 and Aso-2 shards do not overlap (Supplementary material 5). Shards of both spike G18 and Aso-2 are also characterized by very high Co and very high V: >14 and > 161 ppm, respectively (Fig. 7e). Although the shards of spike G18 and the proximal Aso-2 deposits are dissimilar in Rb and Sr contents (Fig. 7c and d), the Rb and Sr contents are positively and negatively related to their K_2O and SiO_2 contents, respectively, in the same way as the Aso-4 components 1−3 of Albert et al. (2019); therefore, G18 and Aso-2 shard chemistries may reflect compositional variation associated with magma evolution. We interpreted spike G18 to be related to the Aso-2 eruptive sequence even though it cannot be directly correlated to the proximal Aso-2 tephra (sample 301). The vertical variation of Aso-2 shard chemistry should be investigated in a future study to ascertain the relationship between distal and proximal Aso-2 deposits.

(2019) obtained by WDS-EPMA were recalculated by the authors to compare with our EDS-EPMA data, and the recalculated ranges are encircled. The shard major-element compositions (average and 1 SD) of Sagawa et al. (2018) obtained by EDS-EPMA are displayed as crosses. The trace-element compositions of Albert et al. (2019) obtained by LA-ICP-MS are also encircled. Error bars on plots represent reproducibility, calculated as 2 SD of replicate analyses of MPI-DING ATHO-G. Outliers not plotted are included in Supplementary material 1. Bi-plots of SiO_2 versus alkali, FeO* versus CaO, and Na_2O versus Al_2O_3 are in Supplementary material 5 d−f.

Fig. 7. Chemical compositions of glass shards from tephras corresponding to MIS 5−6. (a) SiO₂ versus K₂O; (b) Th versus Zr; (c) Th versus Rb; (d) Th versus Sr; (e) Co versus V; and (f) Y versus Sr/Y. The ranges of terrestrial tephras are encircled. Information on the sampled terrestrial tephras is in Table 1. The shard major-element compositions of Schindlbeck et al. (2018) and Albert et al. (2019) obtained by WDS-EPMA were recalculated by authors to compare with our EDS-EPMA data, and the recalculated ranges are encircled. The shard

5.4. MIS 7 to 10 (190−360 ka)

5.4.1. Spike G21 and Ata-Torihama tephra

Spike G21 (36.30−36.38 mbsf) included a large amount of H-type shards, and we observed a visible yellowish-gray ash layer in this horizon (Table 2). The shards are similar to Ata-Th shards from Ata caldera with respect to their SiO_2, K_2O, Th, Zr, and Rb content ranges (Fig. 8) and their FeO*, CaO, Na_2O, and Al_2O_3 content ranges (Supplementary material 5). Therefore, we confirmed the correlation between spike G21 and Ata-Th. The spike G21 horizon corresponds to the reported Ata-Th horizon (36.38−36.41 mbsf; Ikehara et al., 2006) in core MD012422 and is positioned at the transition from MIS 8 to 7 (ca. 240 ka) (Fig. 2), consistent with the reported age of other Ata-Th deposits (Machida and Arai, 2003).

5.4.2. Subspike G22.2 and the Takayama-Ng1 tephra

Subspike G22.2 (40.55−40.60 mbsf) included a large amount of M-type shards, and we observed dark brown patches of fine sand but no tephra layer in this horizon (Table 2). Most shards are similar to Tky-Ng1 shards from the Suiendani source vent or another nearby source in central Japan with respect to their SiO_2, K_2O content ranges (Fig. 8) and other major-element content ranges (Supplementary material 1). Although some subspike G22.1 shards are also similar to Tky-Ng1 (Fig. 8), those shards were probably reworked from the G22.2 horizon, which is about 1 m below the G22.1 horizon (39.40−39.57 mbsf). Therefore, we confidently correlate subspike G22.2 with Tky-Ng1; thus, Tky-Ng1 was first found in Pacific Ocean sediments by this study. Tky-Ng1 is positioned at the transition from MIS 9 to 8 (290−300 ka) in core MD012422 (Fig. 2), consistent with the reported age of terrestrial Tky-Ng1 deposits (Machida and Arai, 2003).

5.4.3. Spike G24 and Kakuto tephra

Spike G24 (44.80−44.85 mbsf) included a large amount of H-type shards, but we did not observe any visible tephra in this horizon (Table 2). The shards are similar to Kkt shards from Kakuto caldera with respect to their SiO_2, K_2O, Th, Zr, and Rb content ranges (Fig. 9) and their other major- and trace-element content ranges (Supplementary material 1). Therefore, we confidently correlate spike G24 to Kkt. The Kkt horizon is at the MIS 10 to 9 transition (330−340 ka) (Figs. 2), .7−3 m lower than the reported Kkt horizon (41.87−42.08 mbsf, mid−late MIS 9; Ikehara et al., 2006) in core MD012422. The stratigraphic position of the Kkt horizon determined in this study is consistent with the reported stratigraphic position of Kkt relative to other tephras (Machida and Arai, 2003).

5.5. Future correlations of spikes and subspikes to tephras

Among uncorrelated spikes and subspikes, several included glass shards with characteristic chemical compositions that should potentially allow them to be correlated to known tephras in a future study.

Subspike G4.1 and G8.1 and spike G22 shards (Fig. 5a 6a, and 8a) are similar to Aso volcano-derived tephra shards (Fig. 4a) with respect to their SiO_2 and K_2O contents. Subspike G4.1, which corresponds to MIS 3 or 4, may be related to the Aso ACP series (Miyabuchi, 2009, 2011). Subspike 8.1 corresponds to reworked Aso-4 because it occurs just above G8.2 (Aso-4: Fig. 2). Spike G22, which corresponds to MIS 8, is not correlated to Aso-1 (MIS 8) because their shard compositions are different (Fig. 8). To date, no

widespread MIS 8 tephra derived from Aso volcano, other than Aso-1, is known. Further, because G22 shards are dominantly L-type, the spike may correlate to a local tephra that was not produced by an explosive eruption.

Each of subspikes G2.2, G22.4, G23.1, and G23.4 included more than two shards with low K_2O content ranges (<2 wt%: Fig. 9a and Supplementary material 1). Comparison with published shard chemical data (e.g. Schindlbeck et al., 2018; Albert et al., 2019) suggests that these low-K_2O shards were potentially derived from a distant volcano (e.g., in the Izu-Bonin, NE Japan, or Kuril volcanic regions).

In a future study, it may be possible to correlate these spikes and subspikes to individual tephras in terrestrial, lacustrine, and marine sediments on the basis of lithologic and stratigraphic information and their shard major- and trace-element compositions.

6. Discussion

6.1. Re-examination of the core MD012422 age model

We established the Late and Middle Pleistocene tephrostratigraphy and cryptotephrostratigraphy of core MD012422, and we correlated tephras in the core to terrestrial tephras (Section 5; Fig. 2). To create a tephra-based age model (Fig. 10), we used depth and age data of the following well-dated tephras: K-Ah, AT, A-Iw, Aso-4, K-Tz, Aso-ABCD, Aso-3ii, Aso-3i, Aso-2, Ata-Th, Tky-Ng1, and Kkt (Section 5). We used the depths of the lower and upper bounds of each tephra horizon, and we also replaced the age ranges of some tephras that Ikehara et al. (2006) had used to construct their age model with ones from our new compilation. We also plotted the reported depth and ^{14}C data of the planktonic foraminifer *G. inflata* from Ikehara et al. (2006). The nannofossil biohorizon, the FAD of *E. huxleyi*, can sometimes be problematic because its stratigraphic age varies among different ocean areas (Raffi et al., 2006; Anthonissen and Ogg, 2012): 265 ka in the eastern Mediterranean, 289 ka in the equatorial Atlantic Ocean, and 291 ka in the equatorial Pacific Ocean (Raffi et al., 2006, Fig. 10). Therefore, for the FAD of *E. huxleyi* in core MD012422, we show the range of stratigraphic ages estimated in different ocean areas. These ages are nearly equal to or older than the age used for this datum plane (268 ka; Thierstein et al., 1977) in the age model of Ikehara et al. (2006) (Fig. 10).

Our tephra-based age model is in accordance with the $\delta^{18}O$ (MIS-boundary)-based age model (Ikehara et al., 2006) from MIS 6 to 9 (130−350 ka), but not with that for MIS 5 (74−130 ka) (Fig. 10). However, the tephra-based age model for MIS 5 is constrained by the well-dated widespread Aso-4 (MIS 5 b) and K-Tz (MIS 5c−5b) tephras, both of which were newly detected by this study; therefore, our new tephra-based age model is reliable. This age model indicates a roughly constant sedimentation rate of ca. 0.08−0.11 m/ky during MIS 5−9, and it is in accordance with two reported biostratigraphic events, the LAD of *G. ruber* and the FAD of *E. huxleyi* (Ikehara et al., 2006).

Further, from mid-MIS 1 to MIS 4 (7−74 ka), the age model is roughly in accordance with the reported ^{14}C data. The sedimentation rate in this interval is 0.22−0.47 m/ky, faster than the rate during MIS 5−9 (Ikehara et al., 2006, Fig. 10). On the other hand, the age model is not in accordance with the reported ^{14}C and calibrated ages of A-Kn and A-Fm (Nagaoka et al., 2001; McLean et al., 2020: Fig. 10 inset). However, if G4, G5, and G6 correlate to SG14-2814 (A-

major-element compositions (average and 1 SD) of Sagawa et al. (2018) obtained by EDS-EPMA are displayed as crosses. The trace-element compositions of Schindlbeck et al. (2018) obtained by LA-ICP-MS are also encircled. Error bars on plots represent reproducibility, calculated as 2 SD of replicate analyses of MPI-DING ATHO-G (a)−(f) and StHs6/80-G (a). Outliers not plotted are included in Supplementary material 1. Bi-plots of SiO_2 versus alkali, FeO* versus CaO, and Na_2O versus Al_2O_3 are in Supplementary material 5 g−i.

19
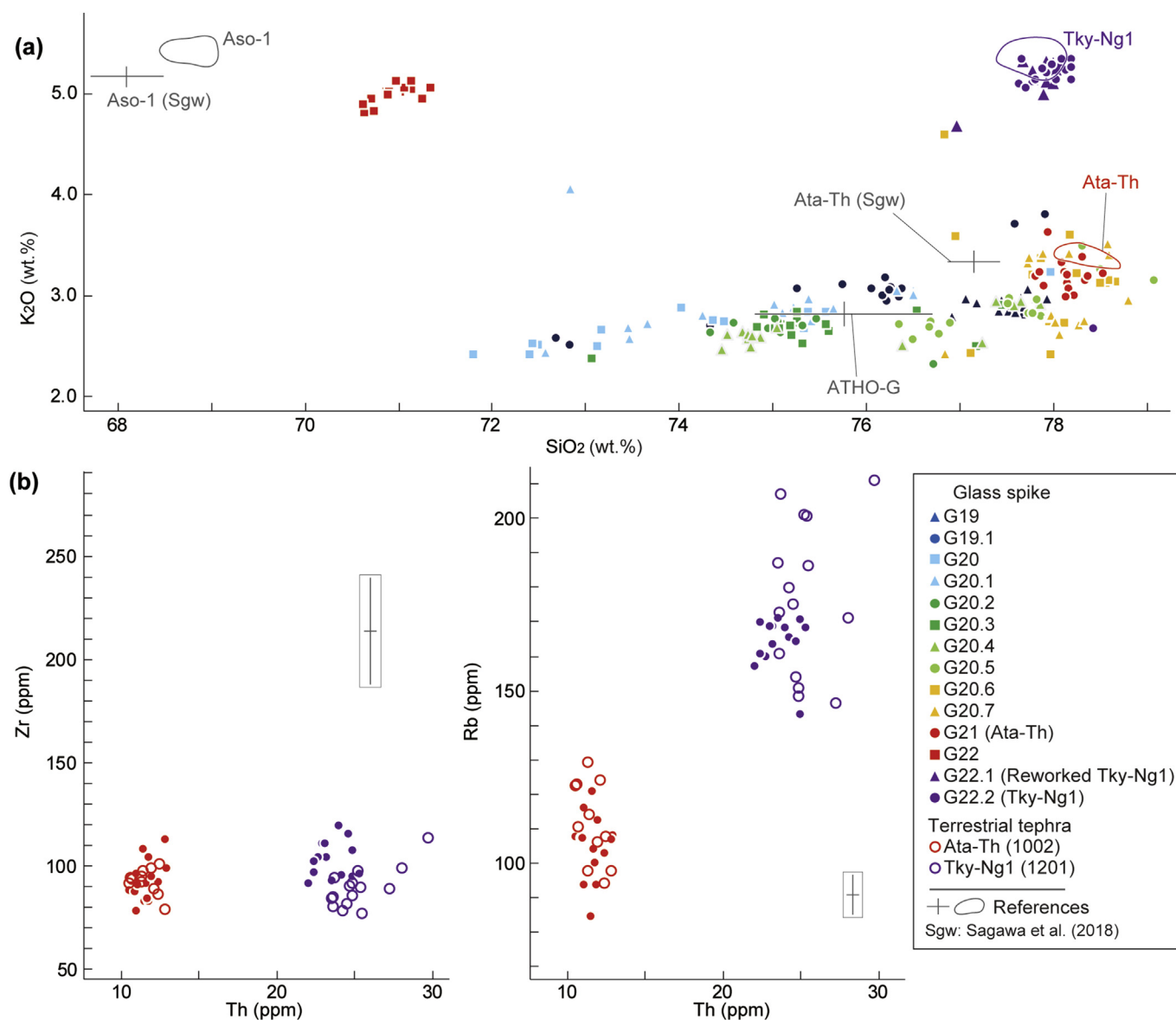
Fig. 8. Chemical compositions of glass shards from tephras corresponding to MIS 6−8. (a) SiO_2 versus K_2O; (b) Th versus Zr; and (c) Th versus Rb. The ranges of terrestrial tephras are encircled. Information on the sampled terrestrial tephras is in Table 1. The shard major-element compositions (average and 1 SD) of Sagawa et al. (2018) obtained by EDS-EPMA are displayed as crosses. Error bars on plots represent reproducibility, calculated as 2 SD of replicate analyses of MPI-DING ATHO-G. Outliers not plotted are included in Supplementary material 1. Bi-plots of SiO_2 versus alkali, FeO* versus CaO, and Na_2O versus Al_2O_3 are in Supplementary material 5j−l.

Kn) and SG14-2856 and −2873 (both A-Fm), respectively, in the Suigetsu tephra series (McLean et al., 2020), as suggested by their shard chemistries and stratigraphic relationships (see section 5.1.3), their ages, based on those determined from Lake Suigetsu sediments, would be 3−4 ka older than the reported ^{14}C and calibrated ages (Fig. 10 inset). The spike G4, G5, and G6 ages based on their correlations to the Suigetsu tephra series are roughly in accordance with our tephra-based age model. In the future, it will be necessary to obtain more data by which to establish a robust correlation of tephras between MD012422 and the Lake Suigetsu cores and Aira tephra series (A-Kn and A-Fm, and also A-Ot, an earlier Aira series tephra). Further, when the age model of the MD012422 core sediments is examined in detail, the sedimentation rate is seen to fluctuate between the G3−G6 and ^{14}C horizons (Fig. 10 inset); therefore, the age model will need to be reconsidered using the newly obtained data.

6.2. Cross-checking the tephrostratigraphy of deep-sea sediments in the NW Pacific area

To improve the marine tephrostratigraphy of the NW Pacific, we used the revised tephrostratigraphy and cryptotephrostratigraphy of core MD012422 to cross-check the reported tephrostratigraphy of Hole U1429 (East China Sea; Sagawa et al., 2018) and Holes U1436A and U1437B (near the Izu-Bonin Islands; Schindlbeck et al., 2018) (Fig. 1b).

6.2.1. Hole U1429

The reported tephras in the sediments of Hole U1429 (East China Sea), corresponding to the last 350 ka, are as follows: K-Ah, Sz-S, AT, Aso-4, K-Tz, Ata, Aso-3, Ata-Th, Aso-1, Kkt, and unknown-a (Sagawa et al., 2018, Fig. 11). All of these tephras, except for tephra unknown-a, are derived from the Kyushu CVR or SVR. Among them, K-Ah, AT, Aso-4, K-Tz, Aso-3, Ata-Th, and Kkt were also detected and
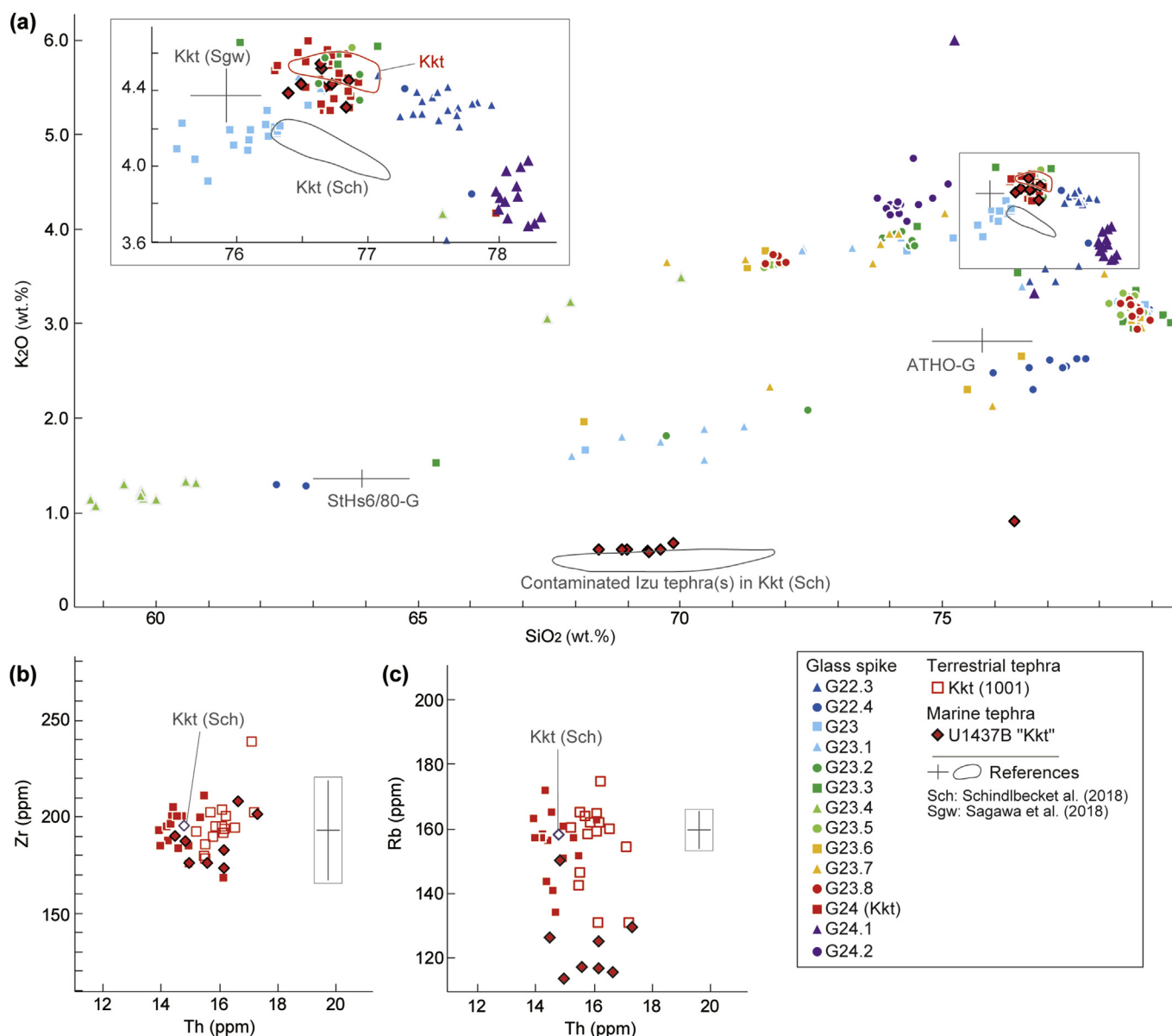
Fig. 9. Chemical compositions of glass shards from tephras corresponding to MIS 8−9. (a) SiO$_2$ versus K$_2$O; (b) Th versus Zr; and (c) Th versus Rb. The ranges of terrestrial tephras are encircled. Information on the sampled terrestrial tephras is in Table 1. The shard major-element compositions of Schindlbecck et al. (2018) obtained by WDS-EPMA were recalculated by authors to compare with our EDS-EPMA data, and the recalculated ranges are encircled. The shard major-element compositions (average and 1 SD) of Sagawa et al. (2018) obtained by EDS-EPMA are displayed as crosses. The trace-element compositions of Schindlbecck et al. (2018) obtained by LA-ICP-MS are also encircled. Error bars on plots represent reproducibility, calculated as 2 SD of replicate analyses of MPI-DING ATHO-G (a)–(c) and StHs6/80-G (a). Outliers not plotted are included in Supplementary material 1. Bi-plots of SiO$_2$ versus alkali, FeO* versus CaO, and Na$_2$O versus Al$_2$O$_3$ are in Supplementary material 5 m−o.

correlated in core MD012422 by this study; therefore, we compared the compositional data of these tephras between Sagawa et al. (2018) and this study (Figs. 5−9). Although the SiO$_2$ contents of these tephras (except Aso-3) reported by Sagawa et al. (2018) are systematically lower than those in our data, other major-element compositions are similar between Sagawa et al. (2018) and our data (Figs. 5−9). Among these tephras, Sagawa et al. (2018) reported that the K-Tz and Aso-3 shards were characterized by bimodal compositional ranges: K-Tz means 1 and 2, and Aso-3 means 1 and 2. Their K-Tz means 1 and 2 correspond to K-Tz and Aso-4, respectively (Fig. 6a); thus, their K-Tz mean 2 is probably contaminated with shards from Aso-4, which is positioned above K-Tz. Aso-3 means 1 and 2 correspond to the bimodal compositional ranges of shards from our terrestrial Aso-3 (601) sample and Aso-

3ii (G16) in core MD012422 (Fig. 7a). Aso-3 in lacustrine sediments in the Takashima-oki core from central Japan (tephra BT39: Nagahashi et al., 2004), and in proximal Aso-3 deposits (Albert et al., 2019), is also reported to have a bimodal compositional range. The Aso-3 array connecting these two modes in the SiO$_2$ and K$_2$O bi-plot (Fig. 7a) has a positive slope with an intercept on the K$_2$O axis intermediate between the intercepts of the Aso-4 and Aso-2 arrays (Fig. 4a). The ages of K-Tz, Ata, Aso-3, Ata-Th, and Kkt in Hole U1429 were reconsidered by Sagawa et al. (2018) with reference to the δ^{18}O stratigraphy, and their ages are roughly consistent with previously known ages (e.g., Machida and Arai, 2003).

6.2.2. Hole U1437B

The following tephras were reported in the sediments of Hole
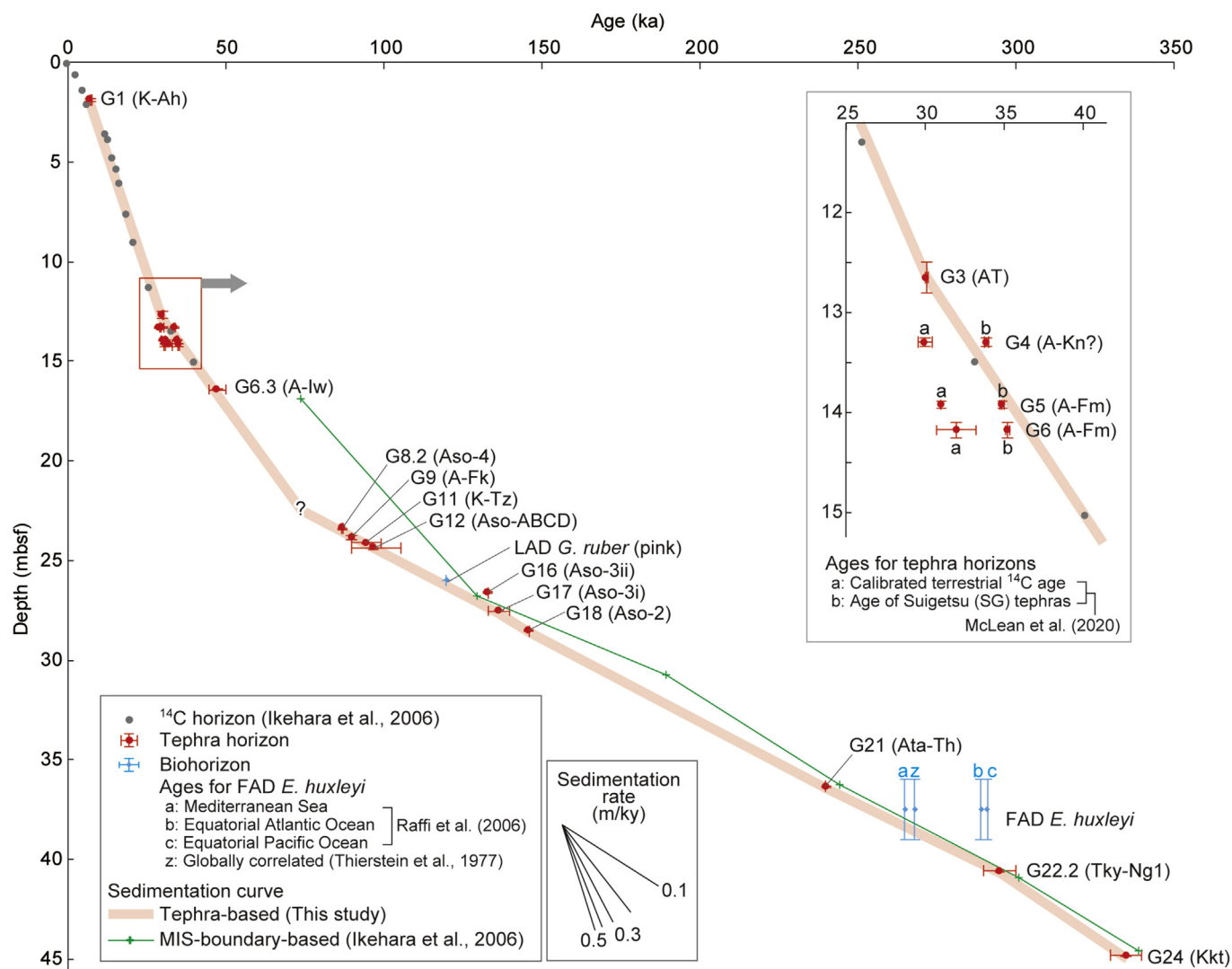
Fig. 10. Age models of the deep-sea sequence in core MD012422. Data for stratigraphic positions of the LAD of *Globigerinoides ruber* (pink) and the FAD of *Emiliania huxleyi* are from Ikehara et al. (2006). The stratigraphic ages of the FAD of *E. huxleyi* are 265 ka in the eastern Mediterranean, 289 ka in the equatorial Atlantic Ocean, and 291 ka in the equatorial Pacific Ocean (Raffi et al., 2006). Tephra ages for spikes G4, G5, and G6 are from calibrated ^{14}C ages based on the terrestrial ^{14}C age data of Nagaoka et al. (2001) and reported by McLean et al. (2020), and from stratigraphic ages based on Lake Suigetsu sediments (McLean et al., 2020), respectively. [14]C ages of Ikehara et al. (2006) were obtained from planktonic foraminifera (*G. inflata*) and calibrated, after taking account of the marine reservoir effect (400 years: Bard et al., 1998), by using CALIB 5.01 (Stuiver and Reimer, 1993) for samples younger than 24 ka, and by using the relationship between coral ages determined by the U–Th and ^{14}C techniques reported by Bard et al. (1998) for samples older than 24 ka. Depth and age data of the datum planes are shown in Supplementary material 8. (For interpretation of the references to colour in this figure legend, the reader is referred to the Web version of this article.)

U1437B (near the Izu-Bonin Islands), roughly corresponding to the last 350 ka: AT, Aso-3, BT51, and Kkt (Schindlbeck et al., 2018, Fig. 11). These tephras are derived from Kyushu volcanic zone, except for BT51, which may be derived from a volcano in NE Japan, as suggested by its glass shard chemistry (Mizuno, 2001; Nagahashi et al., 2015). The reported compositional data of AT, Aso-3, and Kkt in Hole U1437B (hereafter "AT (Sch)", "Aso-3 (Sch)", and "Kkt (Sch)", respectively) are shown in Figs. 5, 7 and 9.

The K$_2$O contents of "AT (Sch)", "Aso-3 (Sch)", and "Kkt (Sch)" are slightly lower than those of AT according to Albert et al. (2019) and this study (Fig. 5a), as well as to those of Aso-3 according to Sagawa et al. (2018), Albert et al. (2019), and this study, and to those of Kkt according to Sagawa et al. (2018) and this study (Fig. 9a). Albert et al. (2019) pointed out that "Aso-3 (Sch)" should be correlated not to Aso-3 but to another Aso volcano-derived tephra, because "Aso-3 (Sch)" has a lower K$_2$O content than Aso-3 tephras with a similar SiO$_2$ content. We confirmed that the composition of

Aso-3 determined in this study is similar to that of Aso-3 as reported by Albert et al. (2019) and dissimilar to "Aso-3 (Sch)" (Schindlbeck et al., 2018), as indicated by Albert et al. (2019) (Fig. 7a). Further, the K$_2$O contents of "AT (Sch)" and "Kkt (Sch)" are slightly lower than those of AT, according to Albert et al. (2019) and this study (Fig. 5a), and those of Kkt, according to Sagawa et al. (2018) and this study (Fig. 9a). Therefore, the K$_2$O contents of the tephra shards in Hole U1437B reported by Schindlbeck et al. (2018) appear to be systematically lower than those reported by other studies. On the other hand, the K$_2$O contents of Aso-4 in Hole U1436A reported by Schindlbeck et al. (2018), which are not lower than those reported for Aso-4 in other studies but well overlap them, do not indicate a systematic error. In addition, the trace-element compositions of "AT (Sch)", "Aso-3 (Sch)", and "Kkt (Sch)" are roughly similar to those of AT, Aso-3, and Kkt, respectively, in this study (Figs. 5, 7 and 9; Supplementary material 2).

For robust tephra correlation between core MD012422 and Hole
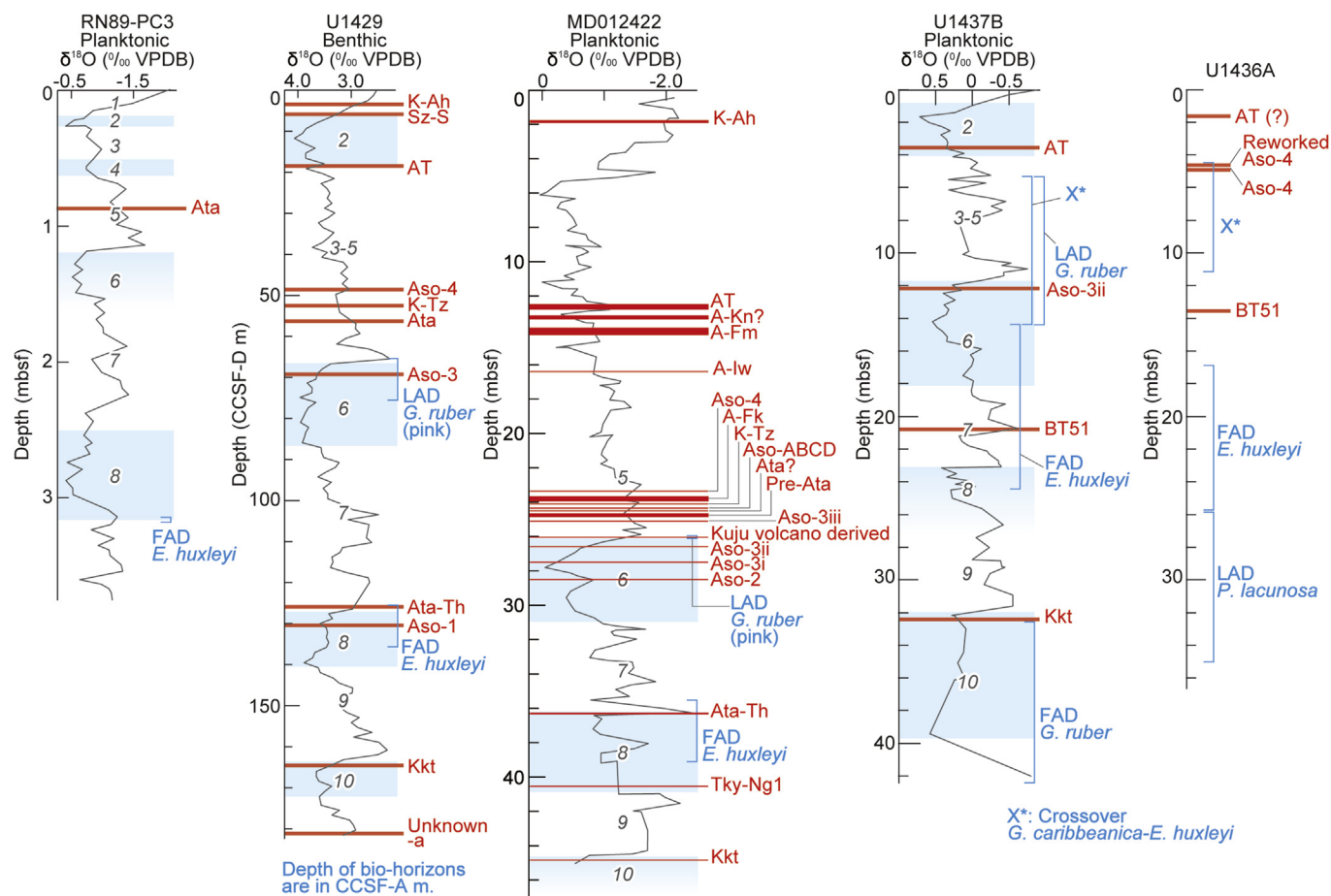
Fig. 11. Stratigraphy, datum planes, and oxygen isotope records of marine sediments in the northwestern Pacific Ocean. Locations of the cores are shown in Fig. 1b. Tephrostratigraphy of the deep-sea sediments: RN89-PC3, Ahagon et al. (1993); Hole U1429, Sagawa et al. (2018); core MD012422, this study; and Holes U1437B and U1436A, Schindlbeck et al. (2018). Aso-4 and Aso-ABCD of Hole U1436A and Aso-3 of Hole U1437B (Schindlbeck et al., 2018) were reassigned to reworked Aso-4, original Aso-4, and Aso volcano-derived tephra, respectively, by Albert et al. (2019). Biostratigraphy of the deep-sea sediments: Hole U1429, Tada et al. (2015); core MD012422, this study; and Holes U1437B and U1436A, Tamura et al. (2015a, b). $\delta^{18}O$ stratigraphy of the deep-sea sediments: Hole U1429, Sagawa et al. (2018); core MD012422, Ikehara et al. (2006); and Hole U1437B, Schindlbeck et al. (2018). The $\delta^{18}O$ stratigraphy of Hole U1436C (Vautravers et al., 2016) is not shown because the age model based on the $\delta^{18}O$ results is not in accordance with the tephra-based age model of Hole 1436 A (Schindlbeck et al., 2018).

U1437B, we newly obtained in our laboratory, using the same analytical procedure as for shards from core MD012422, glass shard chemistries of U1437B "AT", "Aso-3", and "Kkt", collected from the reported tephra horizons of "AT (Sch)", "Aso-3 (Sch)", and "Kkt (Sch)" (U1437B 1H3W50−51, 2H6W78−80, and 4HCC4−8, respectively). In our results, the major-element compositions of U1437B "AT", "Aso-3", and "Kkt" are very similar to those of AT, Aso-3 (Aso-3ii), and Kkt, respectively, in this study and in Sagawa et al. (2018) and Albert et al. (2019) (Figs. 5, 7 and 9), although the U1437B samples also include tephra shards with very low K_2O (~1.5 wt%), probably derived from volcanoes of the Izu-Bonin arc, as reported by Schindlbeck et al. (2018). Although our U1437B "AT" sample was collected from 1 cm above the depth of the AT horizon, U1437B 1H3W51−52, reported by Schindlbeck et al. (2018), we confirmed by a careful core examination that the sampling horizons for AT were the same. The newly obtained shard trace-element composition of U1437B "AT" is also similar to the AT tephra series (except for spike G3 and A-Os) in this study and in Schindlbeck et al. (2018) and Albert et al. (2019) (Fig. 5), and the newly obtained shard trace-element compositions of U1437B "Aso-3", and "Kkt" are similar to Aso-3ii in this study (Fig. 7) and to Kkt in this study and in Schindlbeck et al. (2018) (Fig. 9), respectively. Among these tephra correlations, U1437B "AT" could not be simply correlated to G3 (AT)

in core MD012422 because their U compositions differed subtly (Fig. 5d). This difference indicate that shards of AT tephra units exhibit chemical variations; therefore, AT tephra units should be characterized and discriminated on the basis of their shard trace-element compositions in a future study. Further, although U1437B "Aso-3" was first correlated to Aso-3 (Schindlbeck et al., 2018), that correlation was subsequently rejected (Albert et al., 2019), but we have re-correlated it to Aso-3ii on the basis of our shard chemistry data. In particular, the bimodal composition of U1437B "Aso-3" strongly supports its correlation to Aso-3ii and to terrestrial Aso-3 at location 6 (Fig. 7). The stratigraphic ages of these three correlated tephras indicated by the $\delta^{18}O$ stratigraphy of Hole U1437B appear to be consistent with the known ages of AT, Aso-3ii, and Kkt.

6.2.3. Hole U1436A

The following tephras are reported in the sediments of Hole U1436A (near the Izu-Bonin Islands), roughly corresponding to the last 350 ka: AT, Aso-4, Aso-ABCD, and BT51 (Schindlbeck et al., 2018: Fig. 11). These tephras are derived from the Kyushu volcanic zone (except possibly BT51; see section 6.2.2). The reported compositional data of Aso-4 and Aso-ABCD (hereafter "Aso-4 (Sch)" and "Aso-ABCD (Sch)", respectively) are shown in Fig. 6. Albert et al. (2019) considered "Aso-4 (Sch)" and "Aso-ABCD (Sch)" to be

miscorrelated and re-correlated them to reworked Aso-4 and original Aso-4, respectively, on the basis of their SiO_2 and K_2O contents. The reported compositional ranges of "Aso-4 (Sch)" and "Aso-ABCD (Sch)" are similar to those of Aso-4 according to Sagawa et al. (2018) and this study (Fig. 6a). Our newly obtained shard major-element compositions for U1436A "Aso-4″" and "Aso-ABCD", collected from the "Aso-4 (Sch)" and "Aso-ABCD (Sch)" horizons (U1436A 2H1W25−27 and 2H1W56−58, respectively), are very similar to those of Aso-4 in this study and in Sagawa et al. (2018) and Albert et al. (2019), but not to Aso-ABCD in this study (Fig. 6a); therefore, we confirmed their re-correlation by Albert et al. (2019). Further, the reported AT tephra in Hole U1436A (hereafter "AT (Sch)") is actually a mixed tephra that includes both AT and Izu-Bonin ash shards (Schindlbeck et al., 2018) but which is dominated by Izu-Bonin ash shards (11of 13 shards), as indicated by the major-element compositional data of the shards (Schindlbeck et al., 2018). There are two possible explanations for this mixed tephra: (1) AT shards from an AT horizon close to an Izu-Bonin ash horizon might have contaminated the Izu-Bonin ash, or (2) AT and the Izu-Bonin ash may have erupted simultaneously and have been deposited together to form the "AT (Sch)" horizon. Unfortunately, in U1436A "AT", which we obtained from the "AT (Sch)" horizon (U1436A 1H2W24−27), we could not detect AT shards because all of the U1436A "AT" shards had very low K_2O contents (<1.1 wt%: Fig. 5a). To discuss the true stratigraphic position of the AT horizon, vertical variations of AT shard concentrations near the "AT (Sch)" horizon need to be examined. Despite these problems associated with Hole U1436A tephras, they are important time markers in the Hole U1436A sediments because the detailed $\delta^{18}O$ stratigraphy of the sediments has not been established. However, the $\delta^{18}O$ stratigraphy has been reported for Hole U1436C, 20 m south of Hole U1436A (Vautravers et al., 2016). Therefore, in a future study, the tephrostratigraphy of Hole U1436C should be constructed and integrated with that of Hole U1436A so that the tephra stratigraphic ages can be shared between the two cores.

6.3. Cross-checking age models of marine sequences against globally correlated age indicators

We correlated 15 spikes and subspikes to known tephras, suggested 3 spikes and subspikes were possible correlatives of known tephras, and suggested the possible source volcano of 1 spike. The stratigraphic positions of these tephras in core MD012422 show good agreement with the $\delta^{18}O$ stratigraphy (Section 6.1); therefore, these tephras are useful time-synchronous markers for linking tephrostratigraphy and biostratigraphy in the NW Pacific Ocean area.

Stratigraphic relationships between tephrostratigraphy and biostratigraphy in deep-sea sediments of the NW Pacific Ocean (Holes U1436A and U1437B) and East China Sea (Hole U1429) are shown in Fig. 11. Among the biostratigraphic horizons, one nannofossil biohorizon, the FAD of *E. huxleyi*, has been found in all deep-sea sediments and thus has provided an important control point for age models of deep-sea sequences globally (e.g., Thierstein et al., 1977). The FAD of *E. huxleyi* in core MD012422 occurs in late MIS 8 or early MIS 7, and the horizon overlaps the Ata-Th horizon (Fig. 2). Further, the FAD horizon of *E. huxleyi* (together with Ata-Th) is positioned above Thy-Ng1 (MIS 8/9 transition, 290−300 ka) and Kkt (MIS 9/10 transition, 330−340 ka), and its position is consistent with our age model for MIS 5 to 10 (Fig. 10). Therefore, this FAD horizon is consistent with both the tephrostratigraphy and the $\delta^{18}O$ stratigraphy of the core. Similarly, in the East China Sea (Hole U1429; Tada et al., 2015; Sagawa et al., 2018), near the Ryukyu Islands (core RN89-PC3; Ahagon et al., 1993), and off central Honshu (Holes U1436A and U1437B near the Izu-Bonin

Islands; Tamura et al., 2015a, b; Schindlbeck et al., 2018) (see Fig. 1b), the FAD of *E. huxleyi* is consistent with the $\delta^{18}O$ stratigraphy or the tephrostratigraphy, or both (Fig. 11). Further, the FAD of *E. huxleyi* is consistent with both the $\delta^{18}O$ stratigraphy and microtektite abundance horizons in the South China Sea (Shyu et al., 2001) and the western Philippine Sea (Sun et al., 2011). Therefore, the FAD of *E. huxleyi* in the SW Pacific area may be a globally correlated age indicator (Fig. 11).

In contrast, off northern Honshu (Fig. 1b), the calcareous nannofossil stratigraphy of Holes C9001C, ODP1150A, and ODP1151C (Fig. 1b) occasionally conflicts with the newly obtained tephrostratigraphy for those holes, which is more consistent with the $\delta^{18}O$ stratigraphy and sediment rate chronology of the holes (Matsu'ura et al., 2014, 2017, 2018). Therefore, although age indicators based on the calcareous nannofossil stratigraphy have been widely used (Raffi et al., 2006), their use in age models of marine sequences, especially in the NE Pacific area, requires careful cross-checking (e.g., Takayama et al., 1995). In general, calcareous fossils are not well preserved in the NE Pacific area (e.g., Hagino and Okada, 2003; Domitsu et al., 2010) because the deep waters in that area are corrosive to calcium carbonate (e.g., Berger et al., 1976; Feely et al., 2002, 2004: Fig. 1a). Further, off the Japanese Islands, in the transition zone between the SW (yellow) and NE (blue) Pacific Ocean areas (Fig. 1a), there is regional variation in the preservation of calcareous fossils (e.g., Matsu'ura et al., 2018), probably because the deep waters off northern Honshu are more corrosive to calcium carbonate than the waters off Shikoku Island.

In the future, the tephrostratigraphy and cryptotephrostratigraphy of deep-sea sediments, together with the $\delta^{18}O$ stratigraphy, need to be investigated at many locations in the NW Pacific area to identify reliable isochrons and more tightly constrain biohorizons in order to further examine their global synchronicity or regional variation in this ocean area.

7. Conclusions

We investigated the deep-sea sediments of core MD012422 corresponding to the last 350 ka (since MIS 10) to refine their tephrostratigraphy. We identified tephra and cryptotephra horizons by examining concentrations of glass shards in the sediments of the core. We also sampled relevant terrestrial tephras for comparison. Then we analyzed the major- and trace-element compositions of the glass shards and correlated the tephras and cryptotephras in the core with the terrestrial tephras where possible. Further, we used these results to validate and refine the reported tephrostratigraphy of deep-sea sediments in the NW Pacific Ocean and East China Sea and assessed the relative timing of tephra eruptions and bio-events. Our key results and conclusions are as follows:

We detected 64 glass shard spike and subspikes horizons with high glass shard concentrations in MD012422 core sediments as possible tephras or cryptotephras. The correlated glass spikes and subspikes were originated from the Kyushu volcanic zone (Kuju, Aso, Kakuto, Aira, Ata, and Kikai volcanoes/calderas), except for one subspike with high SiO_2, K_2O, Rb, and Th shards, which was correlated to the Takayama-Ng1 tephra (Tky-Ng1) from Suiendani volcano in central Honshu. As a result, we correlated 15 spikes and subspikes with known tephras, suggested 3 spikes and subspikes were possible correlatives of known tephras, and suggested the possible source volcano of 1 spike. However, some tephra correlations between spikes/subspikes and proximal tephras on Kyushu Island made on the basis of their shard major-element compositions showed subtle variations in their trace-element compositions. Because the shard trace-element compositions may sensitively reflect magma compositional variation, trace-element data for

proximal eruptive units should be obtained for robust tephra correlation.

Using the well-dated tephras, we created a tephra-based age model for core MD012422 and cross-checked the model against the reported biostratigraphy to identify useful time-synchronous markers for this ocean area. In core MD012422, the Ata-Th horizon overlaps with a calcareous nannofossil biohorizon, the first appearance datum (FAD) of *Emiliania huxleyi*. Ata-Th and this FAD biohorizon are stratigraphically above the Tky-Ng1 and Kkt tephras, and this stratigraphic relationship is also observed in deep-sea sediments of the East China Sea and off central Honshu. However, they are not consistent in deep-sea sediments off northern Honshu, where fossils are poorly preserved. This regional variation in the preservation of calcareous fossils is likely because the deep waters off northern Honshu are more corrosive to calcium carbonate than the shallower waters off Shikoku Island.

Declaration of competing interest

The authors declare that they have no known competing financial interests or personal relationships that could have appeared to influence the work reported in this paper.

Appendix A. Supplementary data

Supplementary data to this article can be found online at https://doi.org/10.1016/j.quascirev.2021.106808.

References

Abbott, P.M., Griggs, A.J., Bourne, A.J., Davies, S.M., 2018. Tracing marine cryptotephras in the North Atlantic during the last glacial period: protocols for identification, characterisation and evaluating depositional controls. Mar. Geol. 401, 81–97. https://doi.org/10.1016/j.margeo.2018.04.008.

Ahagon, N., Tanaka, Y., Ujiie, H., 1993. *Florisphaera profunda*, a possible nannoplankton indicator of late Quaternary changes in sea-water turbidity at the northern margin of the Pacific. Mar. Micropaleontol. 22, 255–283.

AIST, National Institute of Advanced Industrial Science and Technology, 2019. Volcanoes of Japan/quaternary volcanoes/volcano by region. https://gbank.gsj.jp/volcano/Quat_Vol/volcano_map.html.

Albert, P.G., Smith, V.C., Suzuki, T., Tomlinson, E.L., Nakagawa, T., McLean, D., Yamada, M., Staff, R.A., Schlolaut, G., Takemura, K., Nagahashi, Y., Kimura, J.-I., Suigetsu, 2006 Project Members, 2018. Constraints on the frequency and dispersal of explosive eruptions at Sambe and Daisen volcanoes (South-West Japan Arc) from the distal Lake Suigetsu record (SG06 core). Earth Sci. Rev. 185 https://doi.org/10.1016/j.earscirev.2018.07.003, 1004-1-28.

Albert, P.G., Smith, V.C., Suzuki, T., McLean, D., Tomlinson, E.L., Miyabuchi, Y., Kitaba, I., Mark, D.F., Moriwaki, H., Nakagawa, T., SG06 Project Members, 2019. Geochemical characterisation of the Late Quaternary widespread Japanese tephrostratigraphic markers and correlations to the Lake Suigetsu sedimentary archive (SG06 core). Quat. Geochronol. 52, 103–131. https://doi.org/10.1016/j.quageo.2019.01.005.

Allan, A.S.R., Baker, J.A., Carter, L., Wysoccanksi, R.J., 2008. Reconstructing the Quaternary evolution of the world's most active silicic volcanic system: insights from an ~1.65 Ma deep ocean tephra record sourced from Taupo Volcanic Zone, New Zealand. Quat. Sci. Rev. 27 (25–26), 2341–2360. https://doi.org/10.1016/j.quascirev.2008.09.003.

Anthonissen, D.E., Ogg, J.G., 2012. Appendix 3–Cenozoic and Cretaceous biochronology of planktonic foraminifera and calcareous nannofossils. In: Gradstein, F.M., Ogg, J.G., Schmitz, M., Ogg, G. (Eds.), The Geologic Time Scale 2012. Elsevier, Amsterdam, pp. 1083–1127.

Aoki, K., 2008. Revised age and distribution of ca. 87 ka Aso-4 tephra based on new evidence from the northwest Pacific Ocean. Quat. Int. 178, 100–118. https://doi.org/10.1016/j.quaint.2007.02.005.

Bard, E., Arnold, M., Hamelin, B., Tisnerat-Laborde, N., Cabioch, G., 1998. Radiocarbon calibration by means of mass spectrometric $^{230}Th/^{234}U$ and ^{14}C ages of corals: an updated database including samples from Barbados, Mururoa and Tahiti. Radiocarbon 40, 1085–1092.

Bassinot, F.C., Labeyrie, L.D., Vincent, E., Quidelleur, X., Shackleton, N.J., Lancelot, Y., 1994. The astronomical theory of climate and the age of the Brunhes–Matuyama magnetic reversal. Earth Planet Sci. Lett. 126, 91–108.

Berger, W.H., Adelseck, C.G., Mayer, L.A., 1976. Distribution of carbonate in surface sediments of the Pacific Ocean. J. Geophys. Res. 81, 2617–2627.

Blockley, S.P.E., Brauer, A., Davies, S.M., Hardiman, M., Harding, P., Lane, C.S., MacLeod, A., Matthews, I., Pyne-O'Donnell, S., Rasmussen, S.O., Wulf, S., Zanchetta, G., 2014. Tephrochronology and the extended INTIMATE (Integration of Ice-core, Marine and Terrestrial records) event stratigraphy 8–128 ka b2k. Quat. Sci. Rev. 106, 88–100. https://doi.org/10.1016/j.quascirev.2014.11.002.

Chun, J.-H., Ikehara, K., Han, S.-J., 2004. Evidence in Ulleung basin sediment cores for a Termination II (penultimate deglaciation) eruption of the Aso-3 tephra. Quat. Res. (Jpn) 43, 99–112.

Davies, S.M., Abbott, P.M., Meara, R.H., Pearce, N.J.G., Austin, W.E.N., Chapman, M.R., Svensson, A., Bigler, M., Rasmussen, T.L., 2014. A North Atlantic tephra framework for 130,000–60,000 years b2k: new tephra discoveries, marine based correlations and future challenges. Quat. Sci. Rev. 106, 101–121. https://doi.org/10.1016/j.quascirev.2014.03.024.

Domitsu, H., Nishi, H., Uchida, J., Oda, M., Ogane, K., Taira, A., Aoike, K., Shimokita Research Group, 2010. Age model of core sediments taken by D/V CHIKYU during the shakedown cruises off Shimokita Peninsula. Kaseki (Fossils, Palaeontol. Soc. Jpn) 87, 47–64. https://doi.org/10.1127/0078-0421/2011/0007 (in Japanese, with English Abstr.).

Feely, R.A., Sabine, C.L., Lee, K., Millero, F.J., Lamb, M.F., Greeley, D., Bullister, J.L., Key, R.M., Peng, T.-H., Kozyr, A., Ono, T., Wong, C.S., 2002. In situ calcium carbonate dissolution in the Pacific Ocean. Global Biogeochem. Cycles 16, 1144. https://doi.org/10.1029/2002GB001866.

Feely, R.A., Sabine, C.L., Lee, K., Berelson, W., Kleypas, J., Fabry, V.J., Millero, F.J., 2004. Impact of anthropogenic CO_2 on the $CaCO_3$ system in the oceans. Science 362–366. https://doi.org/10.1126/science.1097329.

Griggs, A.J., Davies, S.M., Abbott, P.M., Rasmussen, T.L., palmer, A.P., 2014. Optimising the use of marine tephrochronology in the north atlantic: a detailed investigation of the faroe marine ash zones II, III and IV. Quat. Sci. Rev. 106, 122–139. https://doi.org/10.1016/j.quascirev.2014.04.031.

Hagino, K., Okada, H., 2003. Data report: late Quaternary calcareous nannofossils from the northwestern Pacific Ocean, holes 1150A and 1151C, leg 186. In: Suyehiro, K., Sacks, I.S., Acton, G.D., Oda, M. (Eds.), Proc. ODP, Sci. Results, vol. 186, pp. 1–15.

Hopkins, J.L., Millet, M., Timm, C., Wilson, C.J.N., Leonard, G.S., Palin, J.M., Neil, H., 2015. Tools and techniques for developing tephra stratigraphies in lake cores: a case study from the basaltic Auckland Volcanic Field, New Zealand. Quat. Sci. Rev. 123, 58–75. https://doi.org/10.1016/j.quascirev.2015.06.014.

Ikehara, M., Murayama, M., Tadai, O., Hokanishi, N., Daido, N., Kawahata, H., Yasuda, H., 2006. Late Quaternary tephrostratigraphy of two IMAGES cores taken from the off Shikoku in the northwest Pacific. Fossils: The Palaeontological Society of Japan 79, 60–76 (in Japanese, with English abstr.).

Jochum, K.P., et al., 2006. MPI-DING reference glasses for in situ microanalysis: new reference values for element concentrations and isotope ratios. G-cubed 7. https://doi.org/10.1029/2005GC001060.Q02008.

Kamata, H., Danhara, T., Itoh, J., Hoshizumi, H., Kawanabe, Y., 1998. Fission-track ages of zircons in the Miyagi, Shimosakata and Handa pyroclastic-flow deposits erupted from Kuju volcano in central Kyushu, Japan. Bull. Volcanol. Soc. Jpn. 69–73 (in Japanese, with English Abstr.).

Kaneko, K., Inoue, K., Koyaguchi, T., Yoshikawa, M., Shibata, T., Takahashi, T., Furukawa, K., 2015. Magma plumbing system of the Aso-3 large pyroclastic eruption cycle at Aso volcano, Southwest Japan: petrological constraint on the formation of a compositionally stratified magma chamber. J. Volcanol. Geoth. Res. 303, 41–58. https://doi.org/10.1016/j.jvolgeores.2015.07.016.

Kimura, J.-I., Nagahashi, Y., Satoguchi, Y., Chang, Q., 2015. Origins of felsic magmas in Japanese subduction zone: geochemical characterizations of tephras from caldera-forming eruptions<5Ma. G-cubed 16, 2147–2174. https://doi.org/10.1002/2015GC005854.

Kuehn, S.C., Froese, D.G., Shane, P.A.R., INTAV Intercomparison Participants, 2011. The INTAV intercomparison of electron-beam microanalysis of glass by tephrochronology laboratories: results and recommendations. Quat. Int. 246, 19–47. doi:10.1016/j.quaint.2011.08.022.

Lane, C.S., Lowe, D.J., Blockley, S.P.E., Suzuki, T., Smith, V.C., 2017. Advancing tephrochronology as a global dating tool: applications in volcanology, archaeology and palaeoclimatic research. Quat. Geochronol. 40, 1–7. https://doi.org/10.1016/j.quageo.2017.04.003.

Lisiecki, L.E., Raymo, M.E., 2005. A Pliocene-Pleistocene stack of 57 globally

distributed benthic δ^{18}O records. Paleoceanography 20, PA1003. https://doi.org/10.1029/2004PA001071.

Lowe, D.J., 2011. Tephrochronology and its application: a review. Quat. Geochronol. 6, 107–153. https://doi.org/10.1016/j.quageo.2010.08.003.

Machida, H., Arai, F., 2003. Atlas of Tephra in and Around Japan. University of Tokyo Press, Tokyo, p. 336 (in Japanese, with English Abstr.).

Maruyama, S., Danhara, T., Hirata, T., 2017. Re-identification of Shishimuta-Pink tephra samples from the Japanese Islands based on simultaneous major- and trace-element analyses of volcanic glasses. Quat. Int. 456, 180–194. https://doi.org/10.1016/j.quaint.2017.02.024.

Maruyama, S., Takemura, K., Hirata, T., Yamashita, T., Danhara, T., 2020. Major and trace element abundances in volcanic glass shards in visible tephras in SG93 and SG06 drillcore samples from Lake Suigetsu, central Japan, obtained using femtosecond LA–ICP–MS. J. Quat. Sci. 35, 66–80. https://doi.org/10.1002/jqs.3124.

Matsumoto, A., Ui, T., 1997. K-Ar age of Ata pyroclastic flow deposit, southern Kyushu, Japan. Bull. Volcanol. Soc. Jpn. 42, 223–225 (in Japanese).

Matsu'ura, T., Komatsubara, J., 2017. Use of amphibole chemistry for detecting tephras in deep-sea sequences (Chikyu C9001C cores) and developing a middle Pleistocene tephrochronology for NE Japan. Quat. Int. 456, 163–179. https://doi.org/10.1016/j.quaint.2017.02.030.

Matsu'ura, T., Komatsubara, J., 2018. Detection of tephra and cryptotephras using glass shard chemistry within deep-sea sequences (Chikyu C9001C cores), NW Pacific Ocean: a case study for developing Late Pleistocene marine tephrostratigraphy. JAMSTEC Rep. Res. Development 26, 1–20. http://www.jamstec.go.jp/j/pr/publication/jamstec_rrd/img/20170801.pdf.

Matsu'ura, T., Furusawa, A., Shimogama, K., Goto, N., Komatsubara, J., 2014. Late Quaternary tephrostratigraphy and cryptotephrostratigraphy of deep-sea sequences (Chikyu C9001C cores) as tools for marine terrace chronology in NE Japan. Quat. Geochronol. 23, 63–79. https://doi.org/10.1016/j.quageo.2014.06.001.

Matsu'ura, T., Kimura, J.-I., Chang, Q., Komatsubara, J., 2017. Using tephrostratigraphy and cryptotephrostratigraphy to re-evaluate and improve the Middle Pleistocene age model for marine sequences in northeast Japan (Chikyu C9001C). Quat. Geochronol. 40, 129–145. https://doi.org/10.1016/j.quageo.2016.11.001.

Matsu'ura, T., Komatsubara, J., Ahagon, N., 2018. Using Late and Middle Pleistocene tephrostratigraphy and cryptotephrostratigraphy to refine age models of Holes ODP1150A and ODP1151C, NW Pacific Ocean: a cross-check between tephrostratigraphy and biostratigraphy. Quat. Geochronol. 47, 29–53. https://doi.org/10.1016/j.quageo.2018.03.012.

McLean, D., Albert, P.G., Nakagawa, T., Staff, R., Suzuki, T., , Suigetsu, 2016 Project Members, Smith, V.C., 2016. Identification of the Changbaishan 'Millennium' (B-Tm) eruption in the Lake Suigetsu (SG06) sedimentary archive, Japan: synchronisation of hemispheric-wide palaeoclimate archives. Quat. Sci. Rev. 150, 301–307. https://doi.org/10.1016/j.quascirev.2016.08.022.

McLean, D., Albert, P.G., Nakagawa, T., Suzuki, T., Staff, R.A., Yamada, K., Kitaba, I., , SG14 Project Members, Smith, V.C., 2018. Integrating the Holocene tephrostratigraphy for East Asia using a high-resolution cryptotephra study from Lake Suigetsu (SG14 core), central Japan. Quat. Sci. Rev. 183, 36–38. https://doi.org/10.1016/j.quascirev.2017.12.013.

McLean, D., Albert, P.G., Suzuki, T., Nakagawa, T., Kimura, J.-I., Chang, Q., Miyabuchi, Y., Manning, C.J., MacLeod, A., Blockley, S.P.E., Staff, R.A., Yamada, K., Kitaba, I., Yamasaki, A., Haraguchi, T., Kitagawa, J., , SG14 Project Members, Smith, V.C., 2020. Constraints on the timing of explosive volcanism at Aso and Aira calderas (Japan) between 50 and 30 ka: new insights from the Lake Suigetsu sedimentary record (SG14 core). G-cubed. https://doi.org/10.1029/2019GC008874.

Miyabuchi, Y., 2009. A 90,000-year tephrostratigraphic framework of Aso Volcano, Japan. Sediment. Geol. 220 (3–4), 169–189.

Miyabuchi, Y., 2011. Post-caldera explosive activity inferred from improved 67–30 ka tephrostratigraphy at Aso Volcano, Japan. J. Volcanol. Geoth. Res. 205 (3–4), 94–113. https://doi.org/10.1016/j.jvolgeores.2011.05.004.

Mizuno, K., 2001. Long-term volcanic history inferred from Plio-Pleistocene widespread tephras. Chikyukagaku 23, 605–609 (in Japanese).

Mizuno, K., Kikkawa, K., 1991. Consideration on the extent of a Middle Pleistocene tephra, the NG-1 ash in central Japan. Quat. Res. (Jpn) 50, 435–438.

Nagahashi, Y., Yoshikawa, S., Miyakawa, C., Uchiyama, T., Inouchi, Y., 2004. Stratigraphy and chronology of widespread tephra layers during the past 430 kyr in the Kinki District and Yatsugatake Mountains: major element composition of the glass shards using EDS analysis. Quat. Res. (Jpn) 43, 15–35 (in Japanese, with English Abstr.).

Nagahashi, Y., Sato, T., Takeshita, Y., Tawara, T., Kumon, F., 2007. Stratigraphy and chronology of widespread tephra beds intercalated in the TKN-2004 core sediment obtained from the Takano Formation, central Japan. Quat. Res. (Jpn) 46, 305–332 (in Japanese, with English Abstr.).

Nagahashi, Y., Nakai, S., Kikkawa, K., Okudaira, T., Yoshikawa, S., Yoshida, T., 2015. Petrological properties of tephra beds based on the major and trace element composition of volcanic glass shards —a case study of the Osaka Group and the Takashima-oki drilling core sediments in Lake Biwa, Kinki district, Japan—. Earth Science (Chikyu Kagaku) 69, 205–222 (in Japanese, with English Abstr.).

Nagaoka, S., Okuno, M., 2014. Tephra-stratigraphy of Kuju volcano in southwestern Japan. Earth Monthly 36, 281–296 (in Japanese).

Nagaoka, S., Okuno, M., Arai, F., 2001. Tephrostratigraphy and eruptive history of the Aira caldera volcano during 100–30 ka, Kyushu, Japan. J. Geol. Soc. Jpn. 107,

432–450 (in Japanese, with English Abstr.).

Oba, T., 1991. The eruptive age of Aso-4 and Ata tephra on the basis of the oxygen isotopic stratigraphy. Earth Monthly (Gekkan Chikyu) 13, 224–227 (in Japanese).

Ono, K., Matsumoto, Y., Miyahisa, M., Teraoka, Y., Kanbe, N., 1977. Geology of the Taketa District. Quadrangle Series, Scale 1:50,000. Geol. Surv. Japan, p. 145 (in Japanese, with English Abstr.).

Raffi, I., Backman, J., Fornaciari, E., Palike, H., Rio, D., Lourens, L., Hilgen, F., 2006. A review of calcareous nannofossil astrobiochronology encompassing the past 25 million years. Quat. Sci. Rev. 25, 3113–3137. https://doi.org/10.1016/j.quascirev.2006.07.007.

Rasmussen, S.O., Bigler, M., Blockley, S.P., Blunier, T., Buchardt, S.L., Clausen, H.B., Cvijanovic, I., Dahl-Jensen, D., Johnsen, S.J., Fischer, H., Gkinis, V., Guillevic, M., Hoek, W.Z., Lowe, J.J., Pedro, J.B., Popp, T., Seierstad, I.K., Steffensen, J.P., Svensson, A.M., Vallelonga, P., Vinther, B.M., Walker, M.J.C., Wheatley, J.J., Winstrup, M., 2014. A stratigraphic framework for abrupt climatic changes during the Last Glacial period based on three synchronized Greenland ice-core records: refining and extending the INTIMATE event stratigraphy. Quat. Sci. Rev. 106, 14–28. https://doi.org/10.1016/j.quascirev.2014.09.007.

Sagawa, T., Nagahashi, Y., Satoguchi, Y., Holbourn, A., Itaki, T., Gallagher, S.J., Saavedra-Pellitero, M., Ikehara, K., Irino, T., Tada, R., 2018. Integrated tephrostratigraphy and stable isotope stratigraphy in the Japan sea and east China sea using IODP sites U1426, U1427, and U1429, expedition 346 Asian monsoon. Progr. Earth Planet. Sci. 5, 18. https://doi.org/10.1186/s40645-018-0168-7.

Schindlbeck, J.C., Kutterolf, S., Straub, S.M., Andrews, G.D.M., Wang, K.-L., Mleneck-Vautravers, M.J., 2018. One million years tephra record at IODP sites U1436 and U1437: insights into explosive volcanism from the Japan and Izu arcs. Isl. Arc 27 (3). https://doi.org/10.1111/iar.12244.

Seno, T., Sakurai, T., Stein, S., 1996. Can the Okhotsk plate be discriminated from the North American plate? J. Geophys. Res. 101 (B5), 11,305–11,315.

Shyu, J.-P., Chen, M.-P., Shieh, Y.-T., Huang, C.-K., 2001. A Pleistocene paleoceanographic record from the north slope of the Spratly Island, southern China Sea. Mar. Micropaleontol. 42, 61–93.

Smith, V.C., Mark, D.F., Staff, R.A., Blockley, S.P.E., Bronk Ramsey, C., Bryant, C.L., Nakagawa, N., Kim, K.H., Weh, A., Takemura, K., Danhara, T., Suigetsu 2006 Project Members, 2011. Toward establishing precise ^{40}Ar/^{39}Ar chronologies for Late Pleistocene palaeoclimate archives: an example from Suigetsu SG06, Japan. Quat. Sci. Rev. 30, 2845–2850. https://doi.org/10.1016/j.quascirev.2011.06.020.

Smith, V.C., Staff, R.A., Blockley, S.P.E., Bronk Ramsey, C., Nakagawa, T., Mark, D.F., Takemura, K., Danhara, T., Suigetsu, Project Members, 2013. Identification and correlation of visible tephras in the Lake Suigetsu SG06 sedimentary archive, Japan: chronostratigraphic markers for synchronising east Asian/west Pacific palaeoclimatic records across the last 150 ka. Quat. Sci. Rev. 67, 121–137. https://doi.org/10.1016/j.quascirev.2013.01.026.

Stuiver, M., Reimer, P.J., 1993. Extended ^{14}C data base and CALIB 3.0 14C age calibration program. Radiocarbon 35, 215–230.

Sun, S., McDonough, W.F., 1989. Chemical and isotopic systematics of 630 oceanic basalts: implications for mantle composition and processes. In: Saunders, A.D., Norry, M.J. (Eds.), Magmatism in Ocean Basins, p. 631.

Sun, H.J., Li, T.G., Sun, R.T., Yu, X.K., Chang, F.M., Zheng, T., 2011. Calcareous nannofossil bioevents and microtektite stratigraphy in the western Philippine Sea during the Quaternary. Chin. Sci. Bull. 56, 2732–2738.

Tada, R., Murray, R.W., Alvarez Zarikian, C.A., Anderson Jr., W.T., Bassetti, M.-A., Brace, B.J., Clemens, S.C., da Costa Gurgel, M.H., Dickens, G.R., Dunlea, A.G., Gallagher, S.J., Giosan, L., Henderson, A.C.G., Holbourn, A.E., Ikehara, K., Irino, T., Itaki, T., Karasuda, A., Kinsley, C.W., Kubota, Y., Lee, G.S., Lee, K.E., Lofi, J., Lopes, C.I.C.D., Peterson, L.C., Saavedra-Pellitero, M., Sagawa, T., Singh, R.K., Sugisaki, S., Toucanne, S., Wan, S., Xuan, C., Zheng, H., Ziegler, M., 2015. the Expedition 346 Scientists Sites U1428 and U1429. In: Tada, R., Murray, R.W., Alvarez Zarikian, C.A. (Eds.), Proc. IODP, vol. 346. Integrated Ocean Drilling Program), College Station, TX. https://doi.org/10.2204/iodp.proc.346.109.2015.

Takayama, T., Sato, T., Kameo, K., Goto, T., 1995. Quaternary coccolith biostratigraphy and the age of the Pliocene/Pleistocene boundary. Quat. Res. (Jpn) 34, 157–170 (in Japanese, with English Abstr.).

Tamura, I., Suzuki, T., 2001. Correlation between middle Pleistocene widespread tephra ng-1 and Takayama pumice layer distributed in the hida district, central Japan. Quat. Res. (Jpn) 40, 295–305 (in Japanese, with English Abstr.).

Tamura, Y., Busby, C.J., Blum, P., the Expedition 350 Scientists, 2015a. Site U1436. Proceedings of the International Ocean Discovery Program 350. https://doi.org/10.14379/iodp.proc.350.103.2015.

Tamura, Y., Busby, C.J., Blum, P., and the Expedition 350 Scientists, 2015b. Site U1437. Proceedings of the International Ocean Discovery Program 350. https://doi.org/10.14379/iodp.proc.350.104.2015.

Tatsumi, Y., Suzuki-Kamata, K., Matsuno, T., Ichihara, H., Seama, N., Kiyosugi, K., Nakaoka, R., Nakahigashi, K., Takizawa, H., Hayashi, K., Chiba, T., Shimizu, S., Sano, M., Iwamaru, H., Morozumi, H., Sugioka, H., Yamamoto, Y., 2018. Giant rhyolite lava dome formation after 7.3 ka supereruption at Kikai caldera, SW Japan. Sci. Rep. 8, 2753. https://doi.org/10.1038/s41598-018-21066-w.

Thierstein, H.R., Geitzenauer, K.R., Molfino, B., Shackleton, N.J., 1977. Global synchroneity of late Quaternary coccolith datum levels: validation by oxygen isotopes. Geology 5, 400–404.

Tsuji, T., Ikeda, M., Furusawa, A., Nakamura, C., Ichikawa, K., Yanagida, M., Nishizaka, N., Ohnishi, K., Ohno, Y., 2018. High resolution record of Quaternary explosive volcanism recorded in fluvio-lacustrine sediments of the Uwa basin, southwest Japan. Quat. Int. 471, 278–297. https://doi.org/10.1016/

j.quaint.2017.10.016.

Vautravers, M.J., Expedition 350 Scientists, 2016. Data Report: Pleistocene Planktonic Foraminiferal Oxygen and Carbon Stable Isotope Records and Their Use to Improve the Age Model of Hole U1436C Cores Recovered East of the Aogashima Volcano. https://doi.org/10.14379/iodp.proc.350.201.2016.

Wessel, P., Smith, W.H.F., 1998. New, improved version of the Generic Mapping tools released. EOS Trans. AGU 79, 579.

Westgate, J.A., Pearce, N.J.G., Perkins, W.T., Preece, S.J., Chesner, C.A., Muhammad, R.F., 2013. Tephrochronology of the Toba tuffs: four primary glass populations define the 75-ka Youngest Toba Tuff, northern Sumatra, Indonesia. J. Quat. Sci. https://doi.org/10.1002/jqs.2672.